

Monitoring dusty sources in the vicinity of Sagittarius A*

F. Peißker¹, S. E. Hosseini^{1,2}, M. Zajaček^{1,2,3}, A. Eckart^{1,2}, R. Saalfeld¹, M. Valencia-S.¹, M. Parsa^{1,2}, and V. Karas⁴

¹ I.Physikalisches Institut der Universität zu Köln, Zùlpicher Str. 77, 50937 Köln, Germany
e-mail: peissker@ph1.uni-koeln.de

² Max-Planck-Institut für Radioastronomie, Auf dem Hügel 69, 53121 Bonn, Germany

³ Center for Theoretical Physics, Polish Academy of Sciences, Al. Lotnikow 32/46, 02-668 Warsaw, Poland

⁴ Astronomical Institute, Czech Academy of Sciences, Boční II 1401, 14100 Prague, Czech Republic

Received 24 May 2019 / Accepted 15 December 2019

ABSTRACT

Context. Several dusty infrared sources traced on their orbits around Sgr A* with SINFONI and NACO mounted at the VLT/Chile show near-infrared (NIR) excess and Doppler-shifted line emission. We investigate these sources in order to clarify their nature and compare their relationship to other observed NIR objects close to Sgr A*.

Aims. Using SINFONI, we are able to determine the spectroscopic properties of the dusty infrared sources. Furthermore, we can extract spatial and velocity information of these objects. We are able to identify X7, X7.1, X8, G1, DSO/G2, D2, D23, D3, D3.1, D5, and D9 in the Doppler-shifted line maps of the SINFONI $H + K$ data. From our K - and L' -band NACO data, we derive the related magnitudes of the brightest sources located west of Sgr A*.

Methods. For determining the line of sight velocity information and to investigate single emission lines, we used the near-infrared integral field spectrograph SINFONI datasets between 2005 and 2015. For the kinematic analysis, we used NACO datasets from the years between 2002 and 2018. This study was done in the H , K_s , and L' band. From the 3D SINFONI data-cubes, we extracted line maps in order to derive positional information for the sources. In the NACO images, we identified the dusty counterpart of the objects. When possible, we determined the Keplerian orbits and applied a photometric analysis.

Results. The spectrum of the investigated objects show a Doppler-shifted Bry and HeI line emission. For some objects west of Sgr A*, we additionally find [FeIII] line emission that can be clearly distinguished from the background. A one-component blackbody model fits the extracted near-infrared flux for the majority of the investigated objects, with the characteristic dust temperature of 500 K. The photometric derived H - and K_s -band magnitudes are between $\text{mag}_H > 22.5$ and $\text{mag}_K = 18.1_{-0.8}^{+0.3}$ for the dusty sources. For the H -band magnitudes we can provide an upper limit. For the bright dusty sources D2, D23, and D3, the Keplerian orbits are elliptical with a semi-major axis of $a_{D2} = (749 \pm 13)$ mas, $a_{D23} = (879 \pm 13)$, and $a_{D3} = (880 \pm 13)$ mas. For the DSO/G2, a single-temperature and a two-component blackbody model is fitted to the H -, K -, L' -, and M -band data, while the two-component model that consists of a star and an envelope fits its SED better than an originally proposed single-temperature dusty cloud.

Conclusions. The spectroscopic analysis indicates that the investigated objects could be dust-embedded pre-main-sequence stars. The Doppler-shifted [FeIII] line can be spectroscopically identified in several sources that are located between 17:45:40.05 and 17:45:42.00 in Dec. However, the sources with a DEC less than 17:45:40.05 show no [FeIII] emission. Therefore, these two groups show different spectroscopic features that could be explained by the interaction with a non-spherical outflow that originates at the position of Sgr A*. Following this, the hot bubble around Sgr A* consists out of isolated sources with [FeIII] line emission that can partially account for the previously detected [FeIII] distribution on larger scales.

Key words. stars: black holes – stars: abundances – stars: formation – stars: pre-main sequence – galaxies: star formation – Galaxy: center

1. Introduction

At a distance of approximately 8 kpc at the center of the Milky Way, a supermassive black hole (SMBH) named Sagittarius A* (Sgr A*), with a mass of $\sim 4 \times 10^6 M_\odot$, can be found (Eckart & Genzel 1996; Schödel et al. 2002; Genzel et al. 2010; Eckart et al. 2017; Gravity Collaboration 2019). From a scientific point of view, it provides a unique opportunity to understand the dynamical mechanisms of an accreting supermassive black hole. Almost 40 years ago, Wollman et al. (1977) observed radial velocities of several hundred km s^{-1} of ionized gas that suggested the presence of a supermassive black hole. This finding was then underlined by the observation of massive young stars that orbit the SMBH with high velocities (see, e.g., Eckart & Genzel 1996; Ghez et al. 1998). For a long time, it was believed that star formation in the vicinity of Sgr A* is not possible because of the harsh environment. Stellar winds, dense

concentrations of stars, a possible magnetic field, shock waves, the gas densities, and strong radiation are considerable arguments for the lack of in situ star formation.

In contrast, Morris & Serabyn (1996) suggested that the constant inflow of gas might trigger star formation that could play a role when accretion processes are investigated. Following this, the detection of young stars in the Galactic Center, mostly O/B and Wolf Rayet WR stars, indicate a recent star-forming epoch (Eisenhauer et al. 2005; Habibi et al. 2017). Ghez et al. (2003) formulated the “paradox of youth” which is based on the unexpected detection of young stars in the vicinity of Sgr A*.

Gillessen et al. (2012) reported the discovery of a gas cloud named G2 (see e.g., Burkert et al. 2012; Meyer & Meyer-Hofmeister 2012; Schartmann et al. 2012; Scoville & Burkert 2013, for a review) that is moving towards Sgr A*. It is following the gas cloud G1 (Clénet et al. 2005; Pfuhl et al. 2015; Witzel et al. 2017) and it was expected to become dissolved

during periaipse. However, G1, as well as G2, have been detected, during and after the periaipse in 2014, as compact sources, leading to a range of interpretations (Eckart et al. 2013; Witzel et al. 2014; Zajaček et al. 2014; Valencia-S. et al. 2015). Based on these findings, there is a high probability that G2 is a dust-enshrouded star with a possible bow-shock (Shahzamanian et al. 2016; Zajaček et al. 2017). The authors use a radiative transfer model that matches the detected L' - and K -band magnitudes. Based on this they conclude that the detected Doppler-shifted emission source could indeed be a young stellar object (YSO) with a dust envelope. This would be in line with the mentioned recent star formation epoch. To emphasize the dusty and stellar nature of the object, Eckart et al. (2013) named it Dusty S-cluster Object (DSO). To avoid confusion, we refer to this object in the following as DSO/G2. In this work, we present our H - and K -band detection of the DSO/G2. With the known L' - and M -band flux from Gillessen et al. (2012) and Eckart et al. (2013), we fit a two-component (star+dust envelope) model to the data. Additionally, Eckart et al. (2013), Meyer et al. (2014), and most recently Ciurlo et al. (2020) reported several other dusty sources that can be found in the direct vicinity ($\sim 1'' \approx 0.04\text{pc}$) of Sgr A*. In order to investigate the nature of the dusty sources we emphasize in this paper the analysis of the D-complex that consists out of D2 and D3, as well as the newly discovered D23 and D3.1. This complex of dusty sources can be found about one arcseconds to the west of Sgr A*. This region contains several bright sources, whereas the most prominent ones are D2 and D3 (Eckart et al. 2013). At the same time, they are sufficiently far away from other, bright sources. This allows for a detailed investigation of their near-infrared (NIR) excess and opens the door to investigate the relation to their surrounding. We are combining the results of this investigation with already published data (see Lutz et al. 1993; Mužić et al. 2008, 2010; Yusef-Zadeh et al. 2012; Eckart et al. 2013; Meyer et al. 2014; Zajaček et al. 2017, for more information) on other dusty sources to come to conclusions about their nature.

The sources of the D-complex investigated in this study show similar positional and spectroscopically properties as the X7 source (Mužić et al. 2010) and X8 (Peißker et al. 2019). Concerning their brightness, the dusty sources are comparable to G1 (Pfuhl et al. 2015; Witzel et al. 2017) and the DSO/G2 (Eckart et al. 2013; Witzel et al. 2014; Valencia-S. et al. 2015). The spectroscopic analysis of these sources indicates that several dusty sources could be interpreted as YSOs surrounded by a dusty envelope that is generally non-spherical (Zajaček et al. 2014, 2017). The mystery of their origin could be answered via the numerical hydrodynamic simulations of the interaction of molecular clouds that originate from distances of several parsecs. Naoz et al. (2018) showed that stellar binaries add a velocity component to the star population that is comparable to the observed properties of the GC disk. Additionally, Alig et al. (2013) modeled the interaction of a molecular cloud that interacted with a gas disk. The authors discuss that the stellar disks resulting from this interaction could be responsible for the observed young stars and their orbital parameters. However, Jalali et al. (2014) showed that the gravitational influence of Sgr A* could affect the star formation rate inside approaching clouds with an initial mass of several $100 M_{\odot}$. We investigate if other known and unknown sources could possibly contribute to this scenario or if the sources are rather dissolving gas clouds that are formed through other processes (Calderón et al. 2018). Additionally, the spectral analysis shows that next to the HeI and Bry emission lines there is also a Doppler-shifted $^3G-^3H$ [FeIII] multiplet. Based on this finding, we can divide the investigated

sources in the field of view (FOV) of SINFONI into two groups: those with [FeIII] emission and the rest without these iron lines. We investigate whether this finding influences the view on the Sgr A* bubble that is reported by Lutz et al. (1993) and Yusef-Zadeh et al. (2012). Lutz et al. (1993) show the [FeIII] distribution at the position of the mini-cavity (see Fig. 1, upper left image). The authors not only report a bubble around Sgr A* but also a V-shaped bow-shock feature caused by a wind that most probably originates at the position of Sgr A*. Yusef-Zadeh et al. (2012) show several emission lines observed with the Very Large Array (VLA). The presented data also indicate the presence of a bubble around Sgr A*. They additionally report a $2''$ hole in the investigated bubble that is located to the northern side of Sgr A* and resembles the shape of the mini-cavity. The authors discuss a possible wind and wind-wind interaction from Sgr A* (see also Mužić et al. 2010) but also the presence of young massive stars Mužić et al. (2007). Yusef-Zadeh et al. (2012) conclude that wind from Sgr A* explains the observed features. We follow this setting and present observational evidence that underlines the presence of a high ionizing wind that is expected to originate at the position of Sgr A*. Additionally, the D-complex reveals several dusty sources that emphasize the idea that YSOs form in groups in the vicinity of Sgr A*. This process is realized by infalling molecular clumps that disperse after forming a few solar masses main sequence stars (Jalali et al. 2014). We focus our analysis on the brightest sources in this complex because of the high chance of confusion.

We use adaptive optics (AO) for the NACO imaging in the K_S - and L' -band and spectroscopic data from SINFONI with the $H + K$ grating. Both instruments are mounted by the time of the observations at the Very Large Telescope (VLT). Section 2 explains the observations with a short overview of the on-source integration time. We also list the NACO and SINFONI data used in the analysis. Section 3 provides more information about the analysis tools, such as the high- and low-pass filtering. We also explain how to derive positions and velocities from the data. The results are presented in Sect. 4 and discussed in Sect. 5. Our conclusions are presented in Sect. 6. That section also presents a discussion about the impact on the existing dialogue about the origin and nature of the dusty sources that can be found in the S-cluster. It also connects the emission of the objects with the [FeIII] distribution that is located mostly at the mini-cavity.

2. Observations

This section gives a brief overview of the observational conditions, the instrumentation we used, the structure of the data, and the data reduction algorithms we employed. The observations have been carried out between 2002 and 2018 with the VLT as described in the next sections in detail. Usually, the weather conditions were fair with mostly clear skies. The L - and K -band seeing is good overall, with values ranging between $0''.2$ and $1''.2$ measured directly on the Natural Guide Star (NGS) that is used for the SINFONI and NACO observations. For all observations, AO is used with a NGS in order to avoid the cone effect that could influence the data when a Laser Guide Star (LGS) is used.

2.1. SINFONI

SINFONI is a near-infrared integral field spectrograph (IFS) that operates between $1.1\ \mu\text{m}$ – $2.45\ \mu\text{m}$ (see Eisenhauer et al. 2003; Bonnet et al. 2004, for a detailed description). The instrument uses an optical wavelength sensor. The structure of the resulting 3d data cubes is organized in a way that makes it so that two

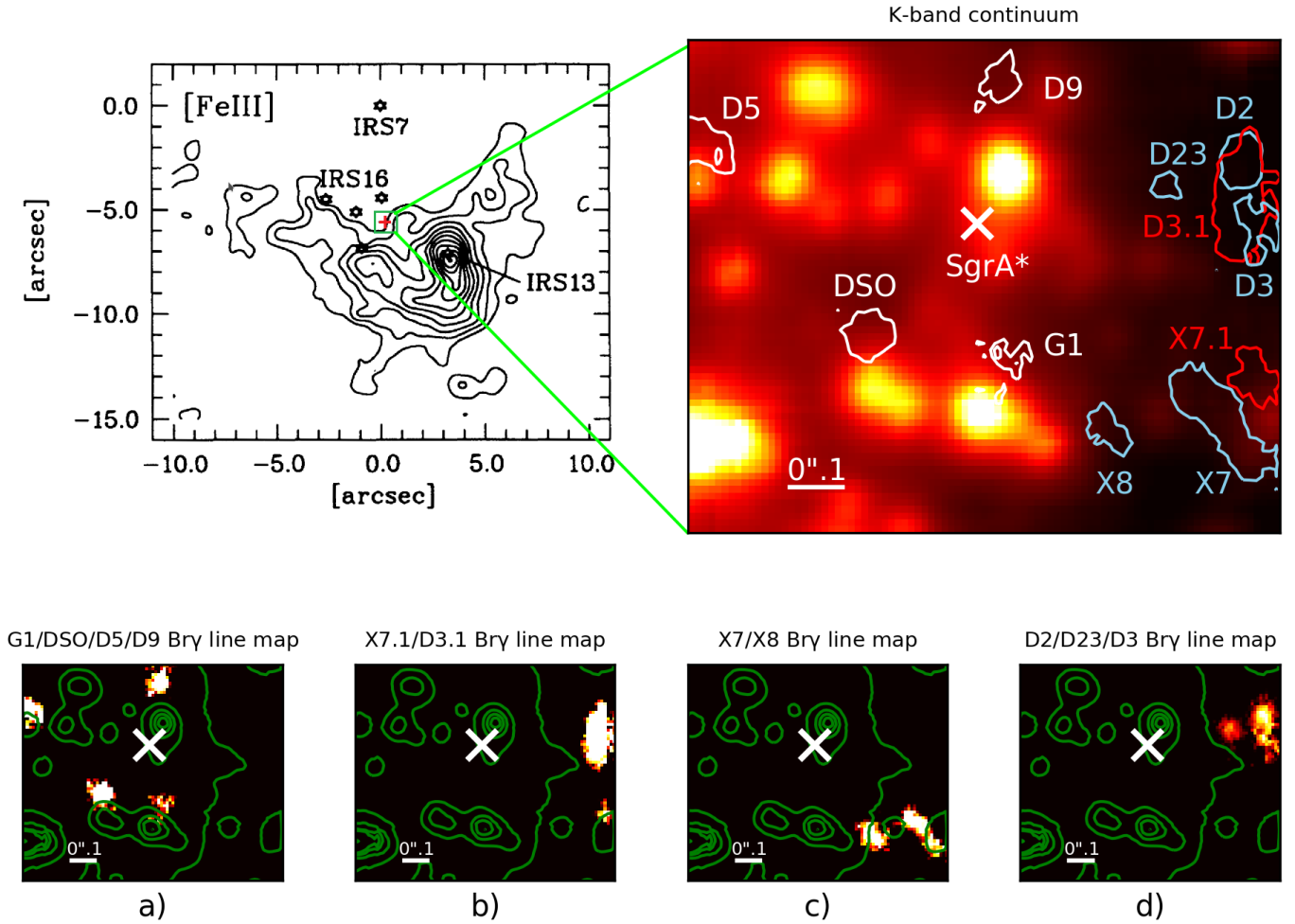


Fig. 1. [FeIII] distribution, K -band continuum, and Doppler-shifted line maps of the GC. North is up, east is to the left in every image. In the upper left corner, a [FeIII] line map adapted from Lutz et al. (1993) is presented. It shows the V-shaped [FeIII] distribution that results in the detection of a bow shock like feature. Also, IRS7, IRS13, and IRS16 are indicated. It is $20''.0 \times 15''.0$ overview where we mark the S-cluster with a green box. Next to the [FeIII] map, a K -band continuum image from the data cube of 2015 is presented. The size of the image matches the green square in the [FeIII] distribution figure next to it and provides a $1''.0 \times 1''.0$ zoom into that region. In this SINFONI K -band continuum image, the contour lines of the, in this work investigated, dusty sources are at 55% of their intensity peak. The white contour lines represent the sources that show no Doppler-shifted [FeIII] emission lines. The blue and red contour lines can be associated with objects that do show Doppler-shifted [FeIII] emission lines. The red and blue color also indicates the Doppler-shift direction. The line maps (a–d) show the dusty sources in 2008 and 2015. Due to the limited FOV of the SINFONI cubes, not all sources are visible in all years. Therefore in (a) we show the 2008 line map to highlight 4 sources. In (b) to (d), we show 2015 line maps to highlight the remaining sources. They are based on the related Doppler shifted Bry line extracted from the SINFONI data cubes. The green contour lines are based on the upper right presented K -band continuum image at 10%, 20%, 30%, 40%, 50%, and 100% of the peak intensity. The related line map velocities, widths, errors, and emission source sizes are listed in Table 1.

dimensions are associated with the spatial x-y plane. Additional spectral information is provided by the third axis of the cube. The Galactic center data is obtained with the $H + K$ grating and enabled AO. We used the smallest plate scale with a FOV of $0''.8 \times 0''.8$ and a spatial pixel scale of $25 \text{ mas pixel}^{-1}$. The AO star we used is located at $15''.54$ north and $8''.85$ east of Sgr A*. The optical magnitude of this star is around $\text{mag} = 14.6$. The detector integration time (DIT) of single exposures is set to 400s in order to individually react to fast-changing weather conditions. Observations that are carried out by other groups have used, in contrast, a DIT setting of 600 s. The subtracted sky is located $5'36''$ north and $12'45''$ west of the central SMBH. Of course, the exposure time setting of the sky fits the object observations and is set to the $H + K$ domain. Prior to the data reduction, we applied a cosmic ray correction (Pych 2004) and a flat field correction to the data. After the standard data reduction (Modigliani et al. 2007), we stacked single data-cubes to increase the

signal-to-noise ratio (S/N, Valencia-S. et al. 2015; Peißker et al. 2019). For that purpose, we used a reference frame created from single exposures. From this, we extracted the positions of several stars (S1, S2, S4, and S62). These coordinates were then used to shift the single exposures in a 100×100 pixel array. The single exposures were calibrated to avoid effects that are caused by the overlapping single data cubes. We selected only the best cubes for the stacking by picking data with a point spread function (PSF) that provides full width at half maximum (FWHM) values of $<6.0\text{--}6.5$ pixel.

2.2. NACO

NAOS+CONICA (NACO) is a near-infrared imager with a spectrograph mode (Lenzen et al. 2003; Rousset et al. 2003). We used the imager mode of NACO to observe the GC in the L' - and in the K_S -band. IRS7, with an K -band magnitude of

Table 1. Bry line map properties related to Fig. 1.

Bry line map properties	G1	DSO	D5	D9	X7.1	D3.1	X7	X8	D2	D23	D3
Velocity in km s ⁻¹	-1195	+1218	+115	-152	+327	+46	-650	-226	-392	-360	-710
FWHM in km s ⁻¹	346	207	318	110	152	124	138	166	152	180	180
Uncertainty in km s ⁻¹	45	11	42	11	17	17	11	17	58	29	17
Measured size in PSF	1.1 ± 0.3	1.0 ± 0.05	-	0.7 ± 0.2	-	-	-	1.5 ± 0.1	0.8 ± 0.05	0.9 ± 0.08	0.8 ± 0.21

Notes. Due to the limited FOV of the SINFONI cubes, not all sources are visible in all years. Therefore for the first 4 sources, the data correspond to 2008, whereas the remainder of the table data corresponds to 2015. The uncertainties representing the standard deviation in km s⁻¹. The measured object size is given in units of the PSF extracted from S2. The given uncertainties are an indication for the data-quality and the not avoidable noise. Some sources are located at the edge of the FOV and could be part of future observations.

7.7 and 5′5 north of Sgr A*, is a suitable AO star (see Fig. 1). The number of exposures used and the total exposure time of the data in K_S -band is listed in Table C.1 with the observation date and project ID. In the auto-jitter template, the jitter box is set to 4′0 with a DIT of 10 sec and the number of DIT (NDIT) set at three. In total, a single Observation Block (OB) contains 42 offset positions. The K -band observations are carried out with the S13 camera. In the AO configuration file, we are setting the dichroic mirror to N20C80 which results in 20 % light for NAOS. The remaining 80% is directed to the detector (CONICA). For this setting, we only use high-quality data with infrared seeing values of <1′0. The spatial range of the L' -band data is set to 27 mas pixel⁻¹ with a FOV of 28″ × 28″. Because of the robustness of the L' observations when it comes to atmospheric influences, we were able to select a wider range of data compared to the K -band domain. Table C.1 is an overview of the used NACO data and lists the observation date, the associated program ID and the number of exposures with the resulting exposure time. The majority of the investigated NACO data is the same as discussed in Mužić et al. (2010), Dodds-Eden et al. (2011), Witzel et al. (2012), Sabha et al. (2012), Shahzamanian et al. (2016), and Parsa et al. (2017).

3. Analysis

In this section, we describe our analyzing techniques and tools. We briefly introduce the flux calibration procedure and present the emission line extraction.

3.1. Line maps

The Doppler-shifted line maps were extracted from the final SINFONI data-cubes that consist of several individual observations (see Tables C.2, C.3, and C.2). By subtracting the continuum, the Doppler-shifted emission lines of the dusty sources can be studied. From the isolated lines, we were able to create line maps of the related source. These maps can also be associated with the line of sight (LOS) velocity. This procedure can reveal the shape of the Doppler-shifted sources but also eliminates the influence of bright stars that are confusing the spatial analysis of these objects.

3.2. Low- and high-pass filter

When it comes to the PSF of the data (NACO and SINFONI), we used the low- and high-pass filter depending on the scientific goal (Lucy 1974; Mužić et al. 2010). For the analysis, this is significant because the GC is a crowded FOV, especially close to Sgr A* (Sabha et al. 2012). A low-pass filter can be used to blur an image, that is, smear out non-linear pixel information.

Unfortunately, this filter also smooths edges of objects that result in a decreased positional accuracy. However, noise can also be associated with low frequencies. Hence, a high-pass filter can be applied in order to isolate signals that are close to the detection limit. It can be used mainly as an edge-detector to determine the positions of stars and decrease the chance of confusion for nearby objects.

We select a 3px Gaussian when we apply the low-pass filter to the SINFONI and NACO data as discussed in Mužić et al. (2010). Followed by this, a 3-pixel Gaussian-shaped FWHM is again used to smooth the data. The size of the Gaussian used should be adjusted to the overall data-quality. The main advantage of the resulting image is reflected in an improved noise level with slightly blurred edges of the stars compared to the input file.

Applying the high-pass filter with the Lucy-Richardson algorithm to the NACO data is discussed in Witzel et al. (2012). A natural PSF is used for the convolution and deconvolution. Starfinder is used to extract the PSF and to apply the high-pass filter. In contrast, this process needs minor adjustments using SINFONI data. First, we are extracting H - and K_S -band images from the collapsed data-cube in a spectral range of 1.45μm–1.9μm and 2.0μm–2.2μm, respectively. Since noise can influence the resulting H - and K -band image, a local background subtraction must be applied. The validity of the subtracted amount is cross-checked with known stellar positions. Also, the number of iterations can be decreased to a level where the possibility of creating artificial sources can be neglected. The major influence on the data is the PSF. Isolated stars that qualify for the extraction of a PSF are rare in the SINFONI FOV of the GC. Most stars in the GC have a close-by companion. Therefore, the wings of these PSF show strong signs of interactions with other nearby stars. Hence, we used an artificial PSF for the convolution and deconvolution process to minimize the influence of overlapping wings in the SINFONI FOV of the GC. It demonstrated that a rotated Gaussian-shaped PSF between 40°–50° with an FWHM of 4.0–4.5 pixel in the x-direction is suitable for the process. We used varying axis ratios between 1.0–1.2 with respect to the x-direction. This delivers the most accurate results when it comes to reference positions of objects in the FOV.

3.3. Orbital fit

Fitting an orbit to the data requires positions and the line-of-sight velocities. Since multiple Doppler-shifted emission lines are detected for the dusty sources, we focus on the Bry peak because of the S/N compared to HeI or [FeIII]. To avoid source-confusion because of the crowded FOV, we identified the investigated sources in the Doppler-shifted Bry line maps extracted from the SINFONI data-cubes. When possible, we verified the spatial information from the SINFONI line maps with L' and K_S

Table 2. H - and K_S -band magnitudes of the three calibrator stars.

Name	Number	H	K_S
S2	3	16.00	14.13
S7	17	17.04	15.14
S10	10	16.23	14.12

Notes. These values are adapted from Schödel et al. (2010).

NACO continuum images. The position of Sgr A* can be determined either by searching for flares in the single SINFONI data-cubes or by using the position of the NIR counterparts of the SiO Maser in the $27 \text{ mas} \times 27 \text{ mas}$ NACO images. From there, the position of Sgr A* with respect to the SiO Maser in the radio-domain can be determined. The procedure is described in detail in Parsa et al. (2017) where the authors applied all necessary corrections discussed in Pfuhl et al. (2015). By using the position of S1, S2, and S4, the position in the SINFONI data-cubes can be extrapolated. By applying a Gaussian fit to the dusty sources in the SINFONI line maps and the NACO L' and K_S continuum images, the distance to the SMBH is measured.

To derive the velocity, the Doppler-shifted Bry and HeI spectral emission lines were fitted with a Gaussian. The fit of the blue and red-shifted lines is done in two steps. First, the continuum spectrum was fitted and subtracted. After that, the various emission lines of the sources and the ambient line emission, for example, Bry at $2.1661 \mu\text{m}$ or HeI at 2.0586 , were fitted with a Gaussian function. These ambient lines were then subtracted from the spectrum and the emission lines of the sources were fitted again without the ambient emission. From this fit, we derived the central wavelength and the Full Width at Half Maximum (FWHM). However, we also compared the line peak values that are in a satisfying agreement with the Gaussian fit. Whenever necessary, we used this approach in order to derive the LOS velocity of the dusty sources. With this spatial and velocity information, we applied a Keplerian fit to the data. The method is described in Parsa et al. (2017) in detail and is briefly outlined in the following.

We used a Keplerian approach in order to model the orbits of the dusty sources. Based on this, we assumed that the motion of the objects is dominated by a stellar counterpart that is shielded by a dusty envelope. However, we used six initial parameters for the orbital fit: semi-major axis, eccentricity, inclination, periaapsis, longitude, and the time t_{closest} of the periaapsis passage. The likelihood function minimizes the residuals for the orbital parameters. Here, the likelihood function is defined as the weighted sum of the squared residuals. It delivers a direct feedback about the quality of the fit. This iterative process was then repeated with adjusted initial parameters.

For all measured LOS velocities discussed in this work, a barycentric and heliocentric correction was automatically applied by the SINFONI pipeline.

3.4. Flux calibration

For the flux determination, the S-star S2 was chosen as a calibrator since it is the brightest and the most isolated star in the S-cluster compared to other candidates. The spectrum of S2 was taken from the SINFONI data cubes with a circular aperture with radius $r = 4$ pixels. From this spectrum, we subtracted a background taken at a nearby region that shows no contamination of stars. From this background aperture, the averaged flux was multiplied by the number of pixels in the S2 aperture and subtracted

from the spectrum taken from S2. We determined the number of counts at $2.2 \mu\text{m}$ from the resulting background subtracted spectrum. Afterward, we transformed the known S2 K_S -band magnitude (Schödel et al. 2010) to the flux density of $9.12 \times 10^{-12} \text{ erg s}^{-1} \text{ cm}^{-2} \mu\text{m}^{-1}$. In this way the flux density for one pixel can be derived. We multiplied this number to the whole data cube, which was thereby flux calibrated. This was done for the SINFONI data cubes between 2005 and 2016.

3.5. Emission lines of the dusty sources

From the flux-calibrated SINFONI data cubes, we created a source spectrum with a 75 mas circular aperture. We used an iris background subtraction where we defined a “ring” around the circular aperture with different inner and outer radii. Comparing this to background apertures placed in a 3–5 pixel distance to the source aperture showed that the circular-annular method (iris subtraction) can be applied more consistently throughout the data analysis because of the crowded environment of Sgr A*. The generated averaged background was then subtracted from the formerly obtained spectrum. We focused on the spectral range between $2.0 \mu\text{m}$ and $2.4 \mu\text{m}$ where we identified several Doppler-shifted isolated Bry and HeI emission lines. To distinguish spectral features of the sources from features of the background, we subtracted the background from the obtained spectrum. The resulting emission peaks were then fitted with a Gaussian. From the integrated fit, the flux was then estimated.

3.6. Photometry

Here we describe the steps that were performed to determine the K - and H -band (upper limit) magnitudes of D2 and D23 from the SINFONI data. We used appropriate calibrator stars that are listed in Table 2 and adapted from Schödel et al. (2010). These three calibrator S-stars S2, S7, and S10 are present in every data cube of the chosen SINFONI FOV between 2005 and 2016. The S-stars we used are located in an area that is not overly crowded so as to avoid spurious flux from other stars. For the calibrator stars and the sources, the counts in an $r = 3$ -pixel aperture were extracted from the median of the SINFONI data-cube. The counts of the detector correspond to the flux of the sources plus the background emission. This background emission has to be subtracted from the continuum SINFONI data cubes for an accurate magnitude calculation. Three sets of backgrounds were created and for each set, the mean value of five apertures with a consistent radius was derived. In this way, the magnitude of D2 and D23 was calculated three times with different backgrounds and within uncertainties of less than 13 mas , differently centered apertures on the sources themselves. Afterward, the mean value of these results was derived. Moreover, the uncertainty of the magnitudes with their standard deviation can be extracted with this procedure. The fluxes of the sources are computed with the magnitudes from Schödel et al. (2010) and the zero fluxes from Tokunaga & Vacca (2007) using

$$F = F_0 \times 10^{-0.4m}, \quad (1)$$

where F_0 donates the zero flux. The background-subtracted counts of the calibrator stars and their fluxes are used to estimate the calibration ratio. Furthermore, the calibration ratio is used to convert the background-subtracted counts of D2 and D23 to obtain their flux. We corrected the fluxes for extinction. The extinction coefficients for both wavelength bands (H - and K_S -band) were adapted from Fritz et al. (2011). It is 4.21 for the H -band and 2.42 for the K_S -band.

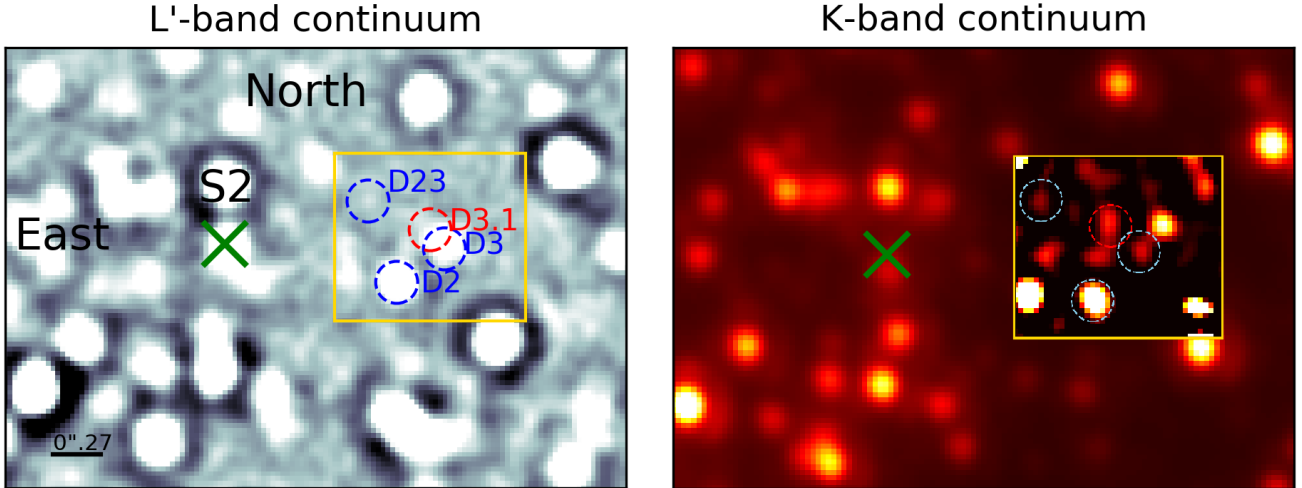


Fig. 2. L - and K -band continuum of the GC in 2006. The approximate position of Sgr A* is indicated by a green x. Above the SMBH, the bright B2V S-star S2 can be found. The D-complex is indicated by a golden rectangle box. At the position of D2 in 2006, the S-star S43 located. However, the L -band flux of S43 is low compared to D2 (flux D2/S43 \sim 2/1). The detected emission in this NACO image is therefore dominated by D2 in 2006. Because of the chosen contrast, D3 and D3.1 appear to be confused. *Right image:* same FOV in the K -band continuum. Even though this image is from 2004, the D-sources are visible at roughly the same position as in the 2006 L' -band image (*left*). Since their magnitudes are close to the detection limit, we use a high- and a low-pass filter to identify a K -band counterpart of the dusty sources. The inlet in the right image shows a 3 px smooth-subtracted detection of these objects.

3.7. Determination of uncertainties

The knowledge of detector-related uncertainties should be considered for a critical evaluation of data points. In the following, we want to frame some of the errors that influence the analysis.

3.7.1. SINFONI

As shown in the SINFONI user manual¹, the shape of a spectral PSF strongly depends on the position of the photons on the detector. This is mainly because the selected pre-optics illuminate the gratings inconsistently. Additionally, the over- and under-subtraction of the sky correction (Davies 2007) play a major role when it comes the identification of compact sources (e.g., the DSO/G2, D23, and G1) that are close to the detection limit. It should also be mentioned that a possible velocity gradient should be analyzed with high caution. Due to image motion, exposures of several hours can lead to rates of more than $\sim 20 \text{ mas hr}^{-1}$ (see Eisenhauer et al. 2003, for more information). This apparent movement of pixels can lead to the false interpretation of a velocity gradient.

In Peißker et al. (2019), we discussed the spectral uncertainty and determine a velocity uncertainty of $0.00048 \mu\text{m}$ or 67 km s^{-1} . Depending on the S/N, it is reasonable to use a positional line map uncertainty of $\pm 20 \text{ mas}$ since this value scales linearly with the total on-source exposure time.

3.7.2. NACO

The spatial uncertainty for the NACO data has already been discussed in Gillessen et al. (2009), Plewa et al. (2015), and Parsa et al. (2017). These authors conclude in their analysis, that using a Gaussian fit the error of stellar positions is better than a tenth of a pixel. Since the spatial pixel scale is 13 mas, this would result in less than 1.3 mas. Because of the crowded environment around Sgr A*, it is reasonable to assume that the error range for K -band positions of the dusty sources should be at least $\pm 6.5 \text{ mas}$. If the

confusion level of the investigated objects is increased because of the close distance to other sources like for example stellar emission or dust, we assume an error range of $\pm 13.0 \text{ mas}$. Since most of the dusty objects show an increased L' magnitude compared to the K_S counterpart, this error range can be reduced even further.

Another source of uncertainties that affect data from both instruments is the position of Sgr A*. In the NACO data, the positional error for the SMBH in the GC ranges from 1 to 2 mas. Using faint flares for positioning can lead to values up to 6 mas. Also, the presence of S17 influences the exact position of Sgr A*. Regarding the SINFONI observations, the data suffer from similar problems. However, since we are combining single exposures of 400s-600s, this process results in data cubes with an integration time of several hours where we detect in almost every year at least one prominent flare.

4. Results

In this section, we present the results of our analysis. As we mentioned before, we emphasize the detection of D2 and D3 since they are the brightest and most isolated members of the sources investigated here. The related spectrum taken from the SINFONI data cubes is presented. Additional flux and magnitude information are also provided, as well as an orbital fit for D2 and D3. Additionally, we present the H - and K -band detection of the DSO/G2 source in 2010 and 2013.

4.1. Sources west of Sgr A*

Here we present known and unknown sources that are located west of Sgr A*.

4.1.1. D2

As reported and discussed in Eckart et al. (2013) and Meyer et al. (2014), we found the dusty source in the blue-shifted Bry line map (Fig. 1). We chose that year because the FOV covers

¹ www.eso.org

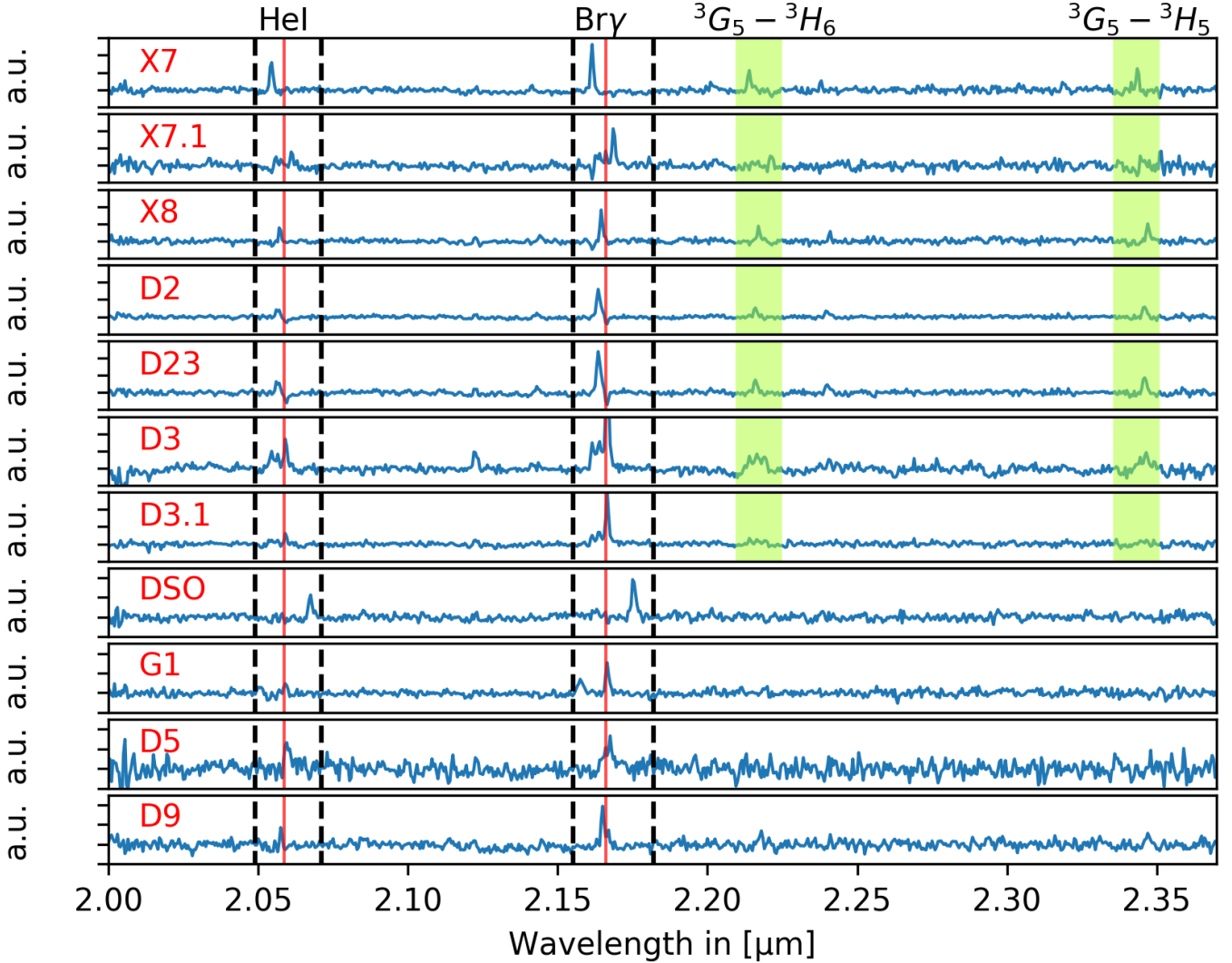


Fig. 3. Spectrum of the dusty sources in the GC in 2008 and 2015. The K -band spectrum between $2.0\mu\text{m}$ and $2.4\mu\text{m}$ is continuum subtracted. The red solid line marks the HeI and Bry rest wavelength at $2.0586\mu\text{m}$ and $2.1661\mu\text{m}$, respectively. The dashed black lines mark the range of the detected blue and red-shifted emission lines. The green bars represent the range of the detected Doppler-shifted [FeIII] lines. The ${}^3G_5-{}^3H_6$ and ${}^3G_5-{}^3H_5$ line are the most prominent of the [FeIII] multiplet. For the purposes of clarity and comprehensibility, the weaker ${}^3G_3-{}^3H_4$ and ${}^3G_4-{}^3H_4$ lines are not marked. We only include the spectra of sources that show a line map counterpart in the SINFONI data cubes. Because of the proper motion of the investigated objects and the limited FOV, the observation of the sources is not possible throughout the entire set of SINFONI data cubes between 2005 and 2016. The intensity of the spectrum is in arbitrary units (a.u.).

D2 and several other sources for comparison in the SINFONI data. As a comparison, Fig. 2 shows the same source in the L' -band in 2006. The error of the positions is between 0.5 – 1.0 pixel in the NACO and SINFONI data-sets that cover the L' - and $H + K$ -band. A positional error, the data quality, and the fit variations are summarized in the resulting uncertainty. The Doppler-shifted Bry and HeI velocities that are detected in the SINFONI data are summarized in Table 4. In Fig. 3, we show the spectrum of D2 in 2015. We find a blue-shifted HeI and Bry peak at $2.0566\mu\text{m}$ and $2.1638\mu\text{m}$. Also, [FeIII] emission lines are detected at $2.1433\mu\text{m}$, $2.2160\mu\text{m}$, $2.2403\mu\text{m}$, and $2.3459\mu\text{m}$ (see Fig. 3). The related velocities can be found in Tables 4 and 5. Also, in Tables D.1 and D.2 we list the K - and L -band positions of the NACO data-sets between 2002 and 2018. Before 2008, the detection of D2 in the K -band NACO data is confused with S43 (see Fig. 2). In contrast, a clear detection of D2 in the L -band is possible for every data-set between 2002 and 2018.

4.1.2. D23

We find this newly discovered source not only in the L' -band NACO images (Fig. 2). The source can also be detected in the blue-shifted Bry line maps. D23 shows several Doppler-shifted K -band emission lines like HeI, Bry, and the [FeIII] multiplet (Tables 3 and 4). In the years between 2014 and 2018, it can be easily confused with D3 (see Table D.1). Unlike D2 and D3, the projected trajectory of the object is directed towards the west. As listed in Table 1, the measured Doppler-shifted Bry line map size is comparable to D2 and D3.

4.1.3. D3

Like D2, this source is part of the analysis in Eckart et al. (2013) and Meyer et al. (2014). D3 shows a blue-shifted Bry velocity of several hundred km s^{-1} (see Table 4). These two Doppler-shifted Bry emission lines are shown in Fig. 3. Like D2 and D23, the

Table 3. Doppler shifted [FeIII] emission lines of D2, D23, and D3.

Source	Spectral line	Central wavelength [μm]	Flux [$10^{-16} \text{ erg s}^{-1} \text{ cm}^{-2}$]
D2	[FeIII] λ 2.145 μm	2.14338 ± 0.00017	4.039 ± 0.009
	[FeIII] λ 2.218 μm	2.21605 ± 0.00016	7.951 ± 0.014
	[FeIII] λ 2.243 μm	2.2403 ± 0.0003	6.392 ± 0.016
	[FeIII] λ 2.348 μm	2.3459 ± 0.0002	11.25 ± 0.03
D23	[FeIII] λ 2.145 μm	$2.14323 \pm 7 \times 10^{-5}$	2.898 ± 0.008
	[FeIII] λ 2.218 μm	$2.21615 \pm 6 \times 10^{-5}$	8.186 ± 0.014
	[FeIII] λ 2.243 μm	2.24006 ± 0.00013	4.661 ± 0.012
	[FeIII] λ 2.348 μm	$2.34580 \pm 8 \times 10^{-5}$	7.171 ± 0.014
D3	[FeIII] λ 2.145 μm	–	–
	[FeIII] λ 2.218 μm	2.21380 ± 0.00017	6.285 ± 0.017
	[FeIII] λ 2.243 μm	–	–
	[FeIII] λ 2.348 μm	2.34450 ± 0.00058	8.893 ± 0.023

Table 4. Line-of-sight velocities of D2, D23, D3, and D3.1.

Year	D2		D23		D3		D3.1	
	v_{HeI} [km s^{-1}]	v_{Bry} [km s^{-1}]	v_{HeI} [km s^{-1}]	v_{Bry} [km s^{-1}]	v_{HeI} [km s^{-1}]	v_{Bry} [km s^{-1}]	v_{HeI} [km s^{-1}]	v_{Bry} [km s^{-1}]
2005	–430	–490	–250	–239	–	–	–	–
2006	–564	–531	–216	–217	–	–	–	–
2007	–523	–479	–226	–215	–	–	–	–
2008	–395	–490	–259	–253	–318	–318	145	116
2009	–458	–440	–	–	–	–	–	–
2010	–377	–410	–243	–257	–	–	131	138
2011	–401	–387	–281	–266	–	–	89	198
2012	–333	–367	–262	–266	–	–	160	152
2013	–353	–349	–292	–284	–	–	136	145
2014	–346	–368	–335	–332	–	–	–	–
2015	–294	–319	–324	–325	–660	–710	58	46
2016	–356	–309	–	–	–	–	–	–

Notes. For D2, D23, and D3.1 we can extract these values directly from the spectroscopic analysis of the SINFONI data cubes. The spectroscopic information for D3 in 2008 are extracted from Meyer et al. (2014). We determine an uncertainty of $0.0005 \mu\text{m}$. This results in a velocity of $\sim 36 \text{ km s}^{-1}$ for the HeI and Bry emission line.

Table 5. Line-of-sight velocities based on the Doppler shifted [FeIII] line emission for D2, D23, and D3 in 2015.

Emission line [μm]	D2		D23		D3	
	RV [km s^{-1}]	σ [km s^{-1}]	RV [km s^{-1}]	σ [km s^{-1}]	RV [km s^{-1}]	σ [km s^{-1}]
2.145	–227	24	–248	10	–	–
2.218	–264	21	–251	9	–676	14
2.243	–357	34	–393	17	–	–
2.348	–265	28	–280	10	–511	63

Notes. The σ is the standard deviation. The ${}^3G-{}^3H$ multiplet is represented by the listed [FeIII] rest emission lines.

blue-shifted [FeIII] lines ${}^3G_5-{}^3H_6$ and ${}^3G_5-{}^3H_5$ can be detected (Table 3). However, the spectroscopic information of D3 is limited to a range of a few years because of the chosen location of the SINFONI FOV. Because of the reduced S/N at the border of the SINFONI data-cube, a detection of the [FeIII] ${}^3G_3-{}^3H_4$ and ${}^3G_4-{}^3H_4$ lines is not possible without confusion.

4.1.4. D3.1

Additionally, we find a source close to D3 that we name (for simplicity) D3.1. The analysis of the L' -band NACO data shows that D3.1 is moving in the same proper direction as the neighboring

source D3. The spectroscopic information extracted from the SINFONI data cube of D3.1 shows a red-shifted Bry line with a velocity of around 50 km s^{-1} close to the Bry rest wavelength in 2015. There are detectable traces of the [FeIII] multiplet but we cannot rule out the possibility of confusing the source spectrum with other close by objects as D2, D23, and D3. However, the clear red-shifted Bry line map detection shows indications of an elongated source close to the mentioned objects (see Fig. 1). The HeI and Bry LOS velocity is listed in Table 4. Because of the close distance of D2, D23, and D3 between 2014 and 2018, a detection in the NACO L' and K -band images is not free of confusion.

Table 6. [FeIII] line map properties related to Fig. 6.

[FeIII] line map properties	X7.1	D3.1	X7	X8	D2	D23	D3
Velocity in km s ⁻¹	+383	-550	-488	-122	-264	-251	-676
FWHM in km s ⁻¹	216	216	162	148	175	94	110
Uncertainty in km s ⁻¹	33	33	20	20	21	9	14

Notes. The blue- and red-shifted line maps are based on the ${}^3G_5-{}^3H_6$ [FeIII] emission line at $2.2178\mu\text{m}$.

4.1.5. X7

The blue-shifted X7 (see Mužić et al. 2007, 2010, for more information) and X8 (Peißker et al. 2019) sources in the GC are spatially close and can be characterized as (slightly) elongated sources that point towards Sgr A*. However, X7 is prominent in the L -band and can be identified in every available NACO data-set. Like X8, the position angle (north-east) of X7 is around $\sim 45^\circ$ and pointing towards Sgr A*. The object contributes to the idea of the existence of an ionizing wind coming from Sgr A* (consider Lutz et al. 1993; Mužić et al. 2010; Yusef-Zadeh et al. 2012). Also, we find blue-shifted HeI and Bry lines with a velocity of around 600 km s^{-1} . The prominent [FeIII] multiplet lines ${}^3G_5-{}^3H_6$ and ${}^3G_5-{}^3H_5$ are shown in Fig. 3 with a similar blue-shifted velocity of around 500 km s^{-1} .

4.1.6. X7.1

We additionally identify another source north of X7 with a projected distance of around $50.0\text{ mas}-100.0\text{ mas}$ that we name X7.1. Because of the S27 NACO camera pixel scale, a confusion-free L' -band identification cannot be guaranteed. This red-shifted source is also close to the projected position of X7. It is furthermore located at the border of the SINFONI data cube where we expect a non-linear behavior for the detector. However, an individual identification of this source is presented in Fig. 1. The related spectrum can be found in Fig. 3. It shows red-shifted HeI and Bry as well as [FeIII] ${}^3G_5-{}^3H_6$ and ${}^3G_5-{}^3H_5$ lines. Since the object is close to the FOV border, measuring the size is not satisfying. The LOS velocity of the ${}^3G_5-{}^3H_6$ and Bry line is around 380 km s^{-1} (see Tables 1 and 6).

4.1.7. X8

As discussed in Peißker et al. (2019), X8 is a slightly elongated Doppler-shifted source that shows signs of bipolar morphology. Compared with X7, both sources share similar projected positions. We derive also, as mentioned before, a comparable position angle (North-East) for X8 of $\sim 45^\circ$. The analyzed K -band spectrum shows Doppler-shifted HeI and Bry lines. Like for X7, the [FeIII] multiplet is detected at $2.1441\mu\text{m}$ (${}^3G_3-{}^3H_4$), $2.2169\mu\text{m}$ (${}^3G_5-{}^3H_6$), $2.2410\mu\text{m}$ (${}^3G_4-{}^3H_4$), and $2.3469\mu\text{m}$ (${}^3G_5-{}^3H_5$) in 2015. The detected velocity for the ${}^3G_5-{}^3H_6$ [FeIII] line is around 120 km s^{-1} whilst the blue-shifted Bry line is at 220 km s^{-1} (see Tables 1 and 6).

4.2. Sources east of Sgr A*

In this subsection, we show the results of the analysis of sources that are located east of Sgr A*.

4.2.1. G1

The spectroscopic analysis of G1 delivers a LOS velocity of around 1200 km s^{-1} at a blue-shifted Bry emission line of

$2.1575\mu\text{m}$ in 2008, which is consistent with Pfuhl et al. (2015) and Witzel et al. (2017). In their work, the authors trace G1 in the K - and L -band. We find the source in the blue-shifted SINFONI line maps in a distance of around 170 mas to Sgr A* in 2008. The compactness is indicated by the measured size of the object (Fig. 1). Doppler-shifted [FeIII] lines are not detected.

4.2.2. DSO/G2

The DSO/G2 is the focal point of many observations (Gillessen et al. 2012, 2019; Witzel et al. 2014; Valencia-S. et al. 2015; Pfuhl et al. 2015) and has a confirmed L' counterpart that is observed with the NACO S27 camera in imaging mode. Based on the H + K -band data-cubes, we find an H -, K -, and L -band continuum counterpart of the DSO/G2 that is presented in Figs. 4 (middle figure), 5, and F.1 taken from Peißker et al. (in prep.). The position of the source is consistent with the line map detection and the L -band observation of the GC. In the presented Bry channel maps, as well as the H - and K -band detection, the emission associated with the DSO/G2 source indicates a rather compact origin (see also Fig. 1). In Fig. 4, we show that the L' -band detection is consistently compact. Besides the prominent Doppler-shifted Bry and HeI emission line detection in the K -band, we cannot confirm additional features in that wavelength domain that could be connected to the DSO/G2 source. We also present stacked K - and H -band continuum images extracted from our data-cubes (Fig. 5). The same continuum images are used for the Lucy-Richardson deconvolution that is presented in Fig. F.1.

4.2.3. D5

The dusty source D5 is presented in Eckart et al. (2013) and also mentioned in Meyer et al. (2014). In Fig. 3, we present a spectrum of this source extracted from the 2008 SINFONI data cube. Like D2 and D3, the proper motion is directed towards North-East in the projected direction of IRS16 (Fig. 1). Because of the on Sgr A* centered FOV of around $1''.0$ and the trajectory of D5, we cannot identify the source after 2009 in the SINFONI data sets. The LOS velocity of D5 can be determined to 60 km s^{-1} with a red-shifted HeI line of $2.0590\mu\text{m}$ in 2008. However, the Doppler-shifted Bry line at $2.1676\mu\text{m}$ can be translated to a LOS velocity of 210 km s^{-1} . D5 is not showing signs of [FeIII] emission lines which is consistent with the spectral analysis presented in Meyer et al. (2014).

4.2.4. D9

The source D9 is newly discovered and can be found North of S2 (see Fig. 2 for the position of the B2V star). Because of the extended wings of the star, the continuum information of D9 is difficult to obtain. However, we are able to trace the blue-shifted Bry and HeI line in the years 2008, 2010, and 2012 (see Figs. 1 and 3). We find an almost constant velocity of 150 km s^{-1} with

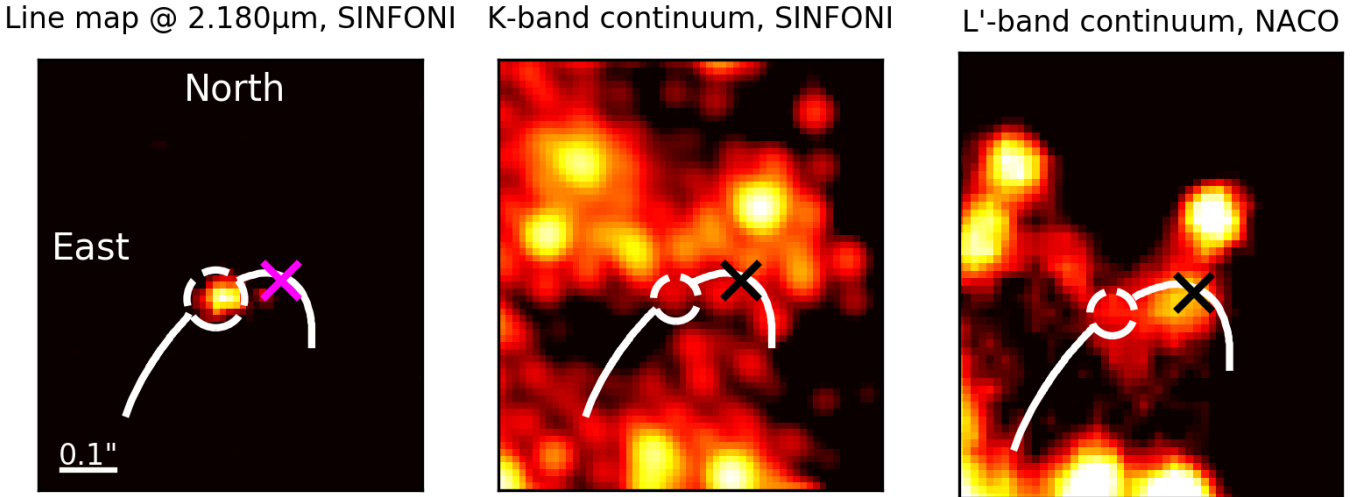


Fig. 4. Galactic center observed in the L - and $H + K$ band with NACO and SINFONI in 2012. North is up, east is to the left. Here, the position of the DSO/G2 is marked with a dashed circle. Sgr A* is located at the position of the “x”. The Keplerian orbital fit is based on the Bry line maps of the DSO/G2 (left image) between 2005 and 2016. The K -band continuum image is a background-subtracted high-pass filtered image with 10 000 iterations. For the convolution and deconvolution process, a Gaussian-shaped APSF is used with an FWHM of 4.7 px. The right image is a cutout of a NACO L -band mosaic observed in 2012 with a pixel scale of 27 mas px⁻¹. The total integration of the NACO image is ~ 450 s, the on-source integration time of the SINFONI cube is ~ 610 min.

a related blue-shifted Bry emission line at $2.1649\mu\text{m}$ (Fig. 1). The blue-shifted HeI line of D9 at $2.05671\mu\text{m}$ is equivalent to 145 km s^{-1} and matches the Bry line velocity. Like G1, DSO/G2, and D5, D9 does not show traces of the [FeIII] multiplet.

4.3. Keplerian orbital fit

Since D2 and D3 are the most prominent and bright dusty sources besides X7 in the vicinity around Sgr A*, we emphasize the analysis of these two objects by fitting a Keplerian orbit to the extracted data points (Tables D.1 and D.2). Nevertheless, during the analysis of D2 and D3, we collect additional information about the two close-by sources D23 and D3.1 (see Fig. A.1). We find that the orbits for at least D2, D3, and D3.1 exhibit a similar orbital shape (see Fig. 9). In contrast, the orientation of the D23 orbit is almost perpendicular to the other members of the “D-complex” and points towards IRS13N. It is also moving clockwise on its projected orbit whilst the other sources are moving counter-clockwise. Because of the distance, a connection between the IRS13 cluster and D23 can be excluded. It is evident that the absolute value of the eccentricity (Table 7) and the LOS velocity (Table 4) for D2, D3 and D3.1 are comparable.

The derived errors (standard deviation) and the orbital parameters (mean values) in Table 7 are based on a variation of the positional data in RA and Dec as well as the FWHM of the resolution of the velocity. In this way, we are including all known and unknown uncertainties.

4.4. Abundance/ionization parameter

We use the [FeIII]/ Bry line ratio as a combined abundance and ionization parameter (AIP) for the detected dusty sources that are located west of the Bry feature (Fig. 6). The orbital parameters of our estimated Keplerian orbit show, that D2, D3, and D3.1 have similar projected trajectories (see Fig. 9). Nonetheless, we find at least for X7, X8, D2, D23, and D3 Doppler shifted [FeIII] lines (see Fig. 3, Peißker et al. (2019), and Meyer et al. 2014). For D3.1, we detect weak traces of the iron emission lines with a ratio of about $D23_{[FeIII]}/D3.1_{[FeIII]} \sim 4$. Table 8

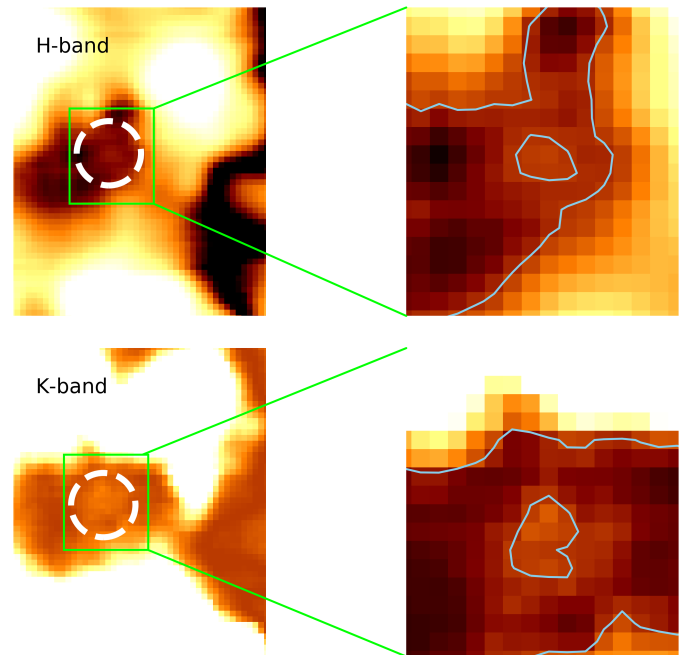


Fig. 5. H - and K -band detection of the DSO/G2 object. Here we stack the continuum images that are used for the Lucy-Richardson detection of the DSO/G2 (see Fig. F.1). We apply for the K - and H -band detection the shifting vector from the Bry detection. The stacked continuum emission in K - and H -band is at the expected position considering the Bry and the Lucy-Richardson deconvolved images. In every image, north is up and east is to the left. The two overview figures to the left are $0':56 \times 0':68$. The two zoomed-in images to the right are $0':18 \times 0':21$. The contour levels are at 80% of the peak intensity of the object at the expected position of the DSO/G2 (right image).

shows the AIP ratio based on the [FeIII]/ Bry flux measurements. We find AIP values for D2, D23, D3, X7, X7.1, and X8 between 24% and 67%. In this sample, X7.1 shows the lowest amount of metal abundance whilst the spectrum of X8 contains

Table 7. Orbital parameters for the dusty sources D2, D23, D3, and D3.1.

Source	a [mpc]	e	i [°]	Ω [°]	ω [°]	t_{closest} [years]
D2	30.01 ± 0.04	0.15 ± 0.02	57.86 ± 1.71	221.16 ± 1.43	44.11 ± 1.14	2002.16 ± 0.03
D23	44.24 ± 0.03	0.06 ± 0.01	95.68 ± 1.14	120.89 ± 3.15	93.39 ± 1.89	2016.00 ± 0.03
D3	35.20 ± 0.01	0.24 ± 0.02	50.99 ± 1.20	206.26 ± 1.76	63.59 ± 2.29	2002.23 ± 0.01
D3.1	31.46 ± 0.01	0.06 ± 0.02	63.02 ± 1.04	47.89 ± 0.96	231.47 ± 1.18	2004.37 ± 0.008

Notes. The given standard deviation is based on the spatial and detector uncertainties.

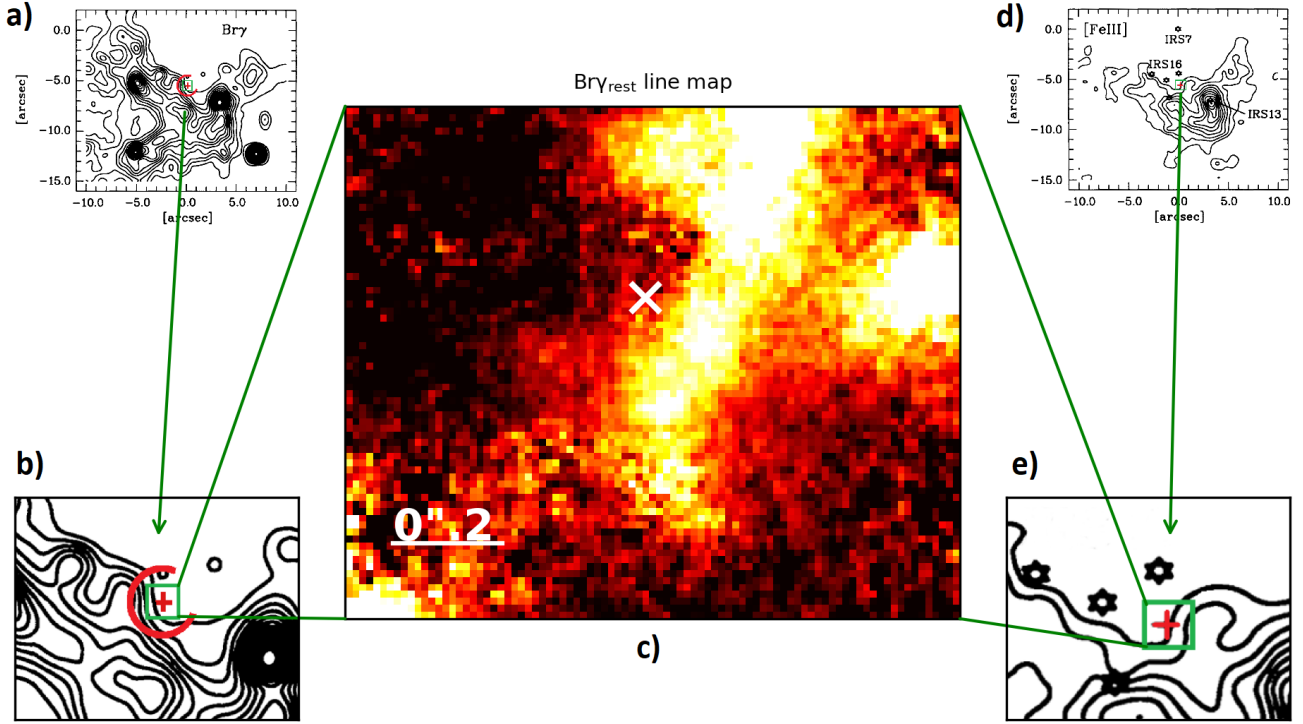


Fig. 6. [FeIII] and Bry line distribution in the Galactic center around Sgr A*. In every image, north is up and east to the left. The scaling of the figures is either mentioned or match the marked squares. *Panel a:* we adapt the Bry detection presented in Lutz et al. (1993) in the GC around Sgr A*. The green box marks the size of the SINFONI FOV. The red circle with the open side towards the west indicates the position of the Sgr A* bubble that is described in detail in Yusef-Zadeh et al. (2012). *Panel b:* zoomed-in figure of (a). Sgr A* is marked with a red cross. *Panel c:* Bry line map at around $2.1661 \mu\text{m}$ extracted from our SINFONI data-cube in 2015. The bright north-south Bry-bar can be detected in every data-cube and is approximately at the position of the open side of the Sgr A* bubble. *Panel d:* [FeIII] distribution around Sgr A*. The [FeIII] line-map emission of the dusty sources around Sgr A* is shown in Fig. B.1. *Panel e:* zoomed-in cutout of (d). The edge of the [FeIII] distribution coincides with the position of the detected Bry-bar shown in (c). From (a) and (b) we can conclude that the [FeIII] emission is significantly decreased inside the Sgr A* bubble. The related velocities, uncertainties, and widths of the [FeIII] line emission are given in Table 6. The phenomena described here are in line with Yusef-Zadeh et al. (2012) (see also Fig. 5 in the mentioned publication and Fig. E.1).

the strongest [FeIII] lines compared to its Bry emission (see Fig. A.3). Depending on the spectrum, we are using either the ${}^3G_5-{}^3H_6$ or ${}^3G_5-{}^3H_5$ transition of the Doppler shifted [FeIII] line (Fig. A.3). By using the [FeIII]/Bry ratio as a function of the Sgr A* offset plot from Lutz et al. (1993) and including the values for X7, X7.1, D2, D23, and D3, we find an increased AIP towards the Galactic center (see Fig. 10).

4.5. Magnitudes of dusty sources

For the photometric analysis of D2, D23, and D3 in the NACO and SINFONI data between 2002 and 2018, we used the calibrator stars S2, S7, and S10 (see Table 2). With the method described in Sect. 3, we derive a K_S -magnitude for the bright sources of the D-complex. For the H -band magnitude, we can estimate an upper limit. For D2, D23, and D3 sources, we find values of $\text{mag}_{H_{\text{up}}} = 22.98$, $\text{mag}_{H_{\text{up}}} = 22.22$, and $\text{mag}_{H_{\text{up}}} = 21.3$

for H -band upper limits, K -band magnitudes of $\text{mag}_K = 18.1$, $\text{mag}_K = 19.7$, and $\text{mag}_K = 19.8$, and L' -band magnitudes of $\text{mag}_{L'} = 13.5$, $\text{mag}_{L'} = 15.13$, and $\text{mag}_{L'} = 13.8$, respectively. Because of the limited SINFONI data sets that show D3 and the chance of interference effects for the flux measurements by the close source D3.1, we adapt the H (upper limit), K , and L' -band magnitude values presented in Eckart et al. (2013). The magnitudes for D2, D23, and D3 can be found in Table 9. The L' -band magnitude of D23 is extrapolated from the D2 and D3 values by using the counts of the source. For that, we derive the ratio of the peak intensity from the emission area of D2 and D23. The resulting peak-count ratio can be used together with

$$\text{mag}_{L'} = -\text{mag}_{S2} + 2.5 \times \log(\text{ratio}), \quad (2)$$

where mag_{S2} donates the extinction corrected S2 L' magnitude of 11.5^2 (Clénet et al. 2001, 2003) and 11.16 (Hosseini et al.,

² Dereddened with $A_K = 2.7$

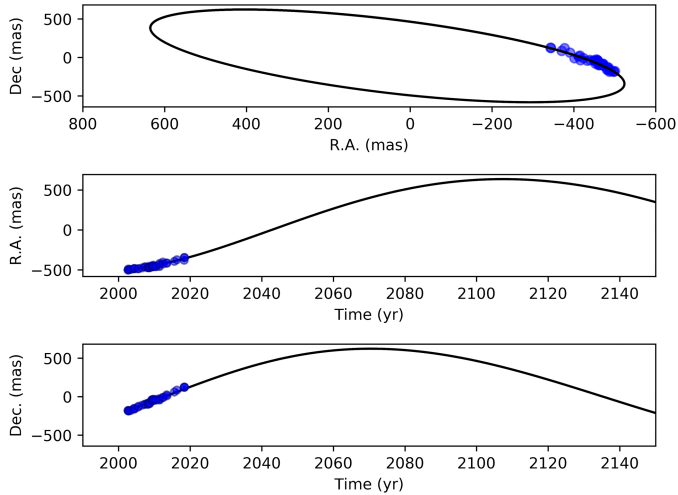


Fig. 7. Orbit of D2. The data used here is extracted from the spectrum extracted from the SINFONI data cube between 2002 and 2018. To enhance the accuracy of the Keplerian fit, we add the NACO L' - and K -band positions of D2.

in prep.; Dereddened with $A_K = 2.4$). The L' magnitude for D23 of $\text{mag}_{L'} = 15.14$ is an average because of the slight variations of the S2 L' magnitude. Using these values and applying a one-component, single-temperature blackbody model, we can reproduce the observed and detected emission (Fig. 11) of D2, D23, and D3 that are presented in the upcoming section.

4.6. SED modeling of dusty sources

We use the flux densities of the studied dusty sources – D2, D23, and D3 – in H , K_S , L' , and M bands to construct their spectral energy distribution (SED) model. First, we fit a one-component, single-temperature blackbody model (BB) to their spectra using the flux-density prescription,

$$S_\nu(R_D, T_D) = (R/d_{GC})^2 \pi B_\nu(T_D), \quad (3)$$

where R_D and T_D are the radius and the temperature of the optically thick photosphere of the dusty sources, respectively, and $B_\nu(T_D)$ is the Planck function. We set the Galactic center distance to $d_{GC} = 8200$ pc, which is consistent with the recent result by the GRAVITY collaboration (Gravity Collaboration 2019). This value is close to the one inferred from S2 star observations with GRAVITY VLTI instrument in K_S -band (Gravity Collaboration 2018). The flux densities in mJy as well as the fitted models for the three dusty objects are depicted in Fig. 11. For all the three sources, the single-temperature BB model fits the continuum flux densities well, with the reduced χ^2_r of 1.51, 11.12, and 5.76 for D2, D23, and D3, respectively. The best-fit parameters along with their 1σ uncertainties are listed in Table 10.

In general, the BB best-fit temperatures for all three sources are the same within the uncertainties $T_D \sim 500$ K, which is most likely due to warm dust heated by the star from inside. The optically thick dust layer has the characteristic black-body length-scale of $R_D \sim 1$ AU, which is also the same for all the objects within the uncertainties.

The temperatures of the investigated objects show a good agreement with the values for the DSO/G2 source (Fig. 4) derived in Eckart et al. (2013) and Zajaček et al. (2017). Here we revisit the blackbody fit of the DSO, including the H -band detection for the first time (see Fig. 12). A single component blackbody fit yields the temperature of $T_{DSO} = 626 \pm 87$ K

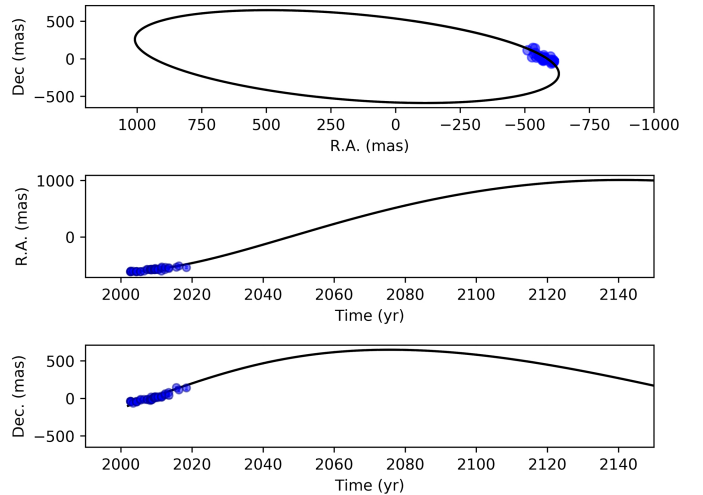


Fig. 8. Orbit of D3. This dusty source is part of the “D-complex” located west of Sgr A*. The used data is based on the NACO L' - and K -band identification of D2. The Doppler-shifted Br γ and He I LOS velocity is adapted from the spectrum presented in Meyer et al. (2014) and the spectroscopic analysis of the SINFONI data cube of 2015.

and the radius of $R_{DSO} = 0.5 \pm 0.3$ AU with the reduced χ^2 of $\chi_r^2 = 6.2$, see also Table 10 for the one component (1C) fit parameters. For this model fit, the H -band flux density is clearly offset and larger than the model-fit value. This motivates an improved, two-component model that consists of a star and its circumstellar envelope. We perform several trial fits, where we fix the SED of a star and search for the temperature and the radius of the surrounding circumstellar envelope. The best-fit with the reduced χ^2 equal to unity is obtained for the star with the effective temperature of 3253 K and the stellar radius equal to one Solar radius. The corresponding best-fit envelope temperature is $T_D = 514 \pm 41$ K and its radius is $R_D = 0.97 \pm 0.31$ AU. In summary, the two-component model including the star significantly improves the aptness of the fit.

The standard classification of young stellar objects (YSOs) is based on the slope α of spectral energy distribution (SED) between $2.2 \mu\text{m}$ and $20 \mu\text{m}$ (Lada et al. 1987), using the prescription $\nu S_\nu \propto \lambda^\alpha$, which can be calculated between K and L' bands as follows,

$$\alpha \equiv \frac{\log(\nu_{L'} S_{L'} / \nu_K S_K)}{\log(\lambda_{L'} / \lambda_K)}. \quad (4)$$

Using Eq. (4), we calculate the spectral slope between K and L' bands for the dusty sources, see Table 10. According to Lada et al. (1987), D2, D23, and D3 would be YSOs of type I, since their derived spectral slope is $\alpha \gg 0.3$. Thus, dusty sources studied in this paper could represent young stars embedded in optically thick dusty envelopes, which can explain the prominent NIR-excess between K_S - and L' -bands, see Fig. 11. This is underlined by the Keplerian orbit (Fig. 9) and the not present evaporation effects caused by the high ionizing environment around Sgr A*. For the D23 and D3 source, the upper limit of the flux density in H_s -band is larger than the corresponding fitted value, which could hint the contribution from the stellar photosphere in a similar way as for the DSO, see Fig. 12 (right panel). For the DSO, the $K - L'$ -band slope is similarly inverted, $\alpha = 4.15$, as for other D-sources which is quite distinct from the stellar SED slope of $\alpha \approx -2$.

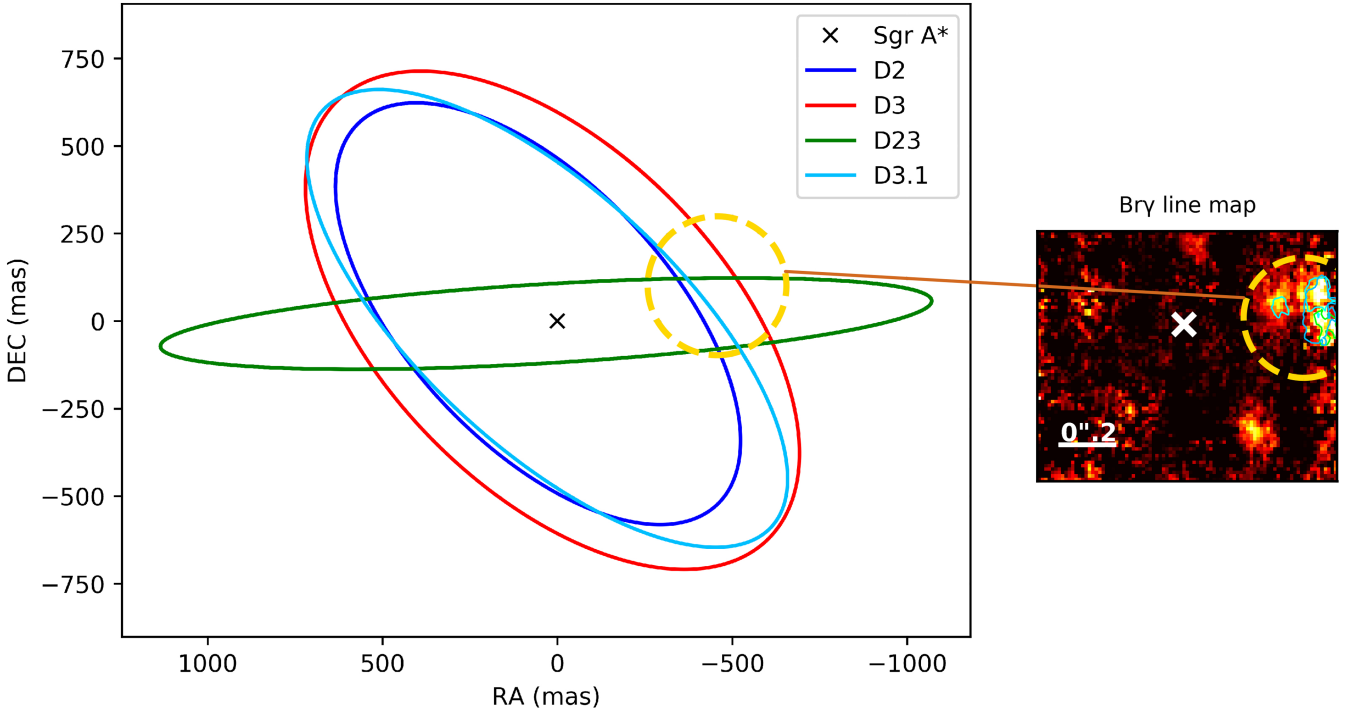


Fig. 9. Orbit of D2, D23, D3, and D3.1. The Keplerian fit is based on the data presented in Tables D.1 and D.2. The dashed circle indicates the investigated area in the SINFONI data cubes. The Doppler-shifted Bry line map shows the emission of D2, D23, and D3 (underlined by 50% peak intensity contour lines). In the line map, north is up, east to the *left*. We do not show the line map of D3.1 since it would dominate the emission of the other sources (for this, consider Fig. 1).

Table 8. Abundance and ionization parameter based on the [FeIII]/Bry integrated line ratio in 2015.

Source	AIP in [%]
X7	36
X7.1	24
X8	67
D2	26
D23	35
D3	44

4.7. Implications for the nature of D-objects

D-sources are located inside the S-cluster with an approximate radius of $r_{\text{cluster}} = 1'' \sim 0.04$ pc. Their blackbody temperature of ~ 500 K, which was determined in the previous section, is larger than the typical temperature of ~ 200 – 300 K of dusty filaments in the innermost parsec, namely the minispiral arms and dust around infrared sources IRS3 and IRS7 (Cotera et al. 1999), see also the illustration in Fig. 13. Given the number of S-stars – around $N \sim 30$, the mean distance is expected to be $\bar{l} \sim r_{\text{cluster}}/N^{1/3} \sim 0.01$ pc = 2700 AU. If there is any dusty clump or filament, its temperature due to external irradiation is given by (Barvainis 1987),

$$T_{\text{dust}} = 9.627 \left[\left(\frac{L_{\text{UV}}}{L_{\odot}} \right) \left(\frac{r_{\text{d}}}{1 \text{ pc}} \right)^{-2} \exp(-\tau_{\text{UV}}) \right]^{1/5.6} \text{ K}, \quad (5)$$

where L_{UV} is the UV luminosity of the central source expressed in Solar luminosity, r_{d} is the dust distance from the source, and τ_{UV} is the optical depth. Considering the S2 star, its bolometric luminosity was inferred to be $L_{\text{S2}} = 10^{4.26} L_{\odot}$ (Habibi et al.

2017), from which we calculate the UV luminosity in the UV wavelength range of $\lambda = 1 - 400$ nm, $L_{\text{UV}} = 10^{4.23} L_{\odot}$. For this luminosity, and using Eq. (5) in the optically thin case, we get the dust temperature of $T_{\text{dust}} = 260$ K, which is consistent with the warmest dust sources in the Galactic Center region (Cotera et al. 1999).

Therefore, the higher temperature of the D-sources implies the presence of an internal source of heating, that is, a star with the UV luminosity of less than $10 L_{\odot}$, which gives the sublimation radius of $r_{\text{sub}} \approx 1.5$ AU. The stellar parameters that we inferred in the best model fit for the DSO – $T_{\star} = 3253$ K and $R_{\star} = 1 R_{\odot}$ – meet this criterion since the overall stellar bolometric luminosity is $L_{\star} = 4\pi R_{\star}^2 \sigma T_{\star}^4 = 0.1 L_{\odot}$ and the UV luminosity is $L_{\text{UV}} = 4 \times 10^{-4} L_{\odot}$. By inverting Eq. (5), we obtain the sublimation radius $r_{\text{sub}}(T_{\text{dust}} = 1000 \text{ K}) = 0.009$ AU and the dust temperature of $T_{\text{dust}} = 500$ K is reached at $r_{\text{d}}(T_{\text{dust}} = 500 \text{ K}) = 0.065$ AU, that is well within the overall extent of the DSO, $R_{\text{DSO}} \sim 1$ AU.

The bolometric luminosity of the dusty envelope then is $L_{\text{env}} = 4\pi R_{\text{env}}^2 \sigma T_{\text{env}}^4 = 2.6 L_{\odot}$, hence, it clearly dominates the overall luminosity of the DSO. In this context, the D-sources could be low-luminosity, light young stars of type I that are remnants of the most recent star-formation episode in the inner parsec of the Galactic center. It is not clear whether they manifest a single separate star-formation epoch, such as due to an infall of a cloud from the more distant regions in the Central Molecular Zone, or rather they formed from the material left-over from the formation of OB stars in an accretion disc ~ 5 million years ago (Levin & Beloborodov 2003) that is a secondary population of lighter objects formed from compressed wind-swept shells. The presence of low-mass stars still surrounded by primordial accretion material in the OB associations in the Galactic plane is observationally well-established (Briceño et al. 2007). While massive OB stars evolve fast on the main sequence at 5 Myr,

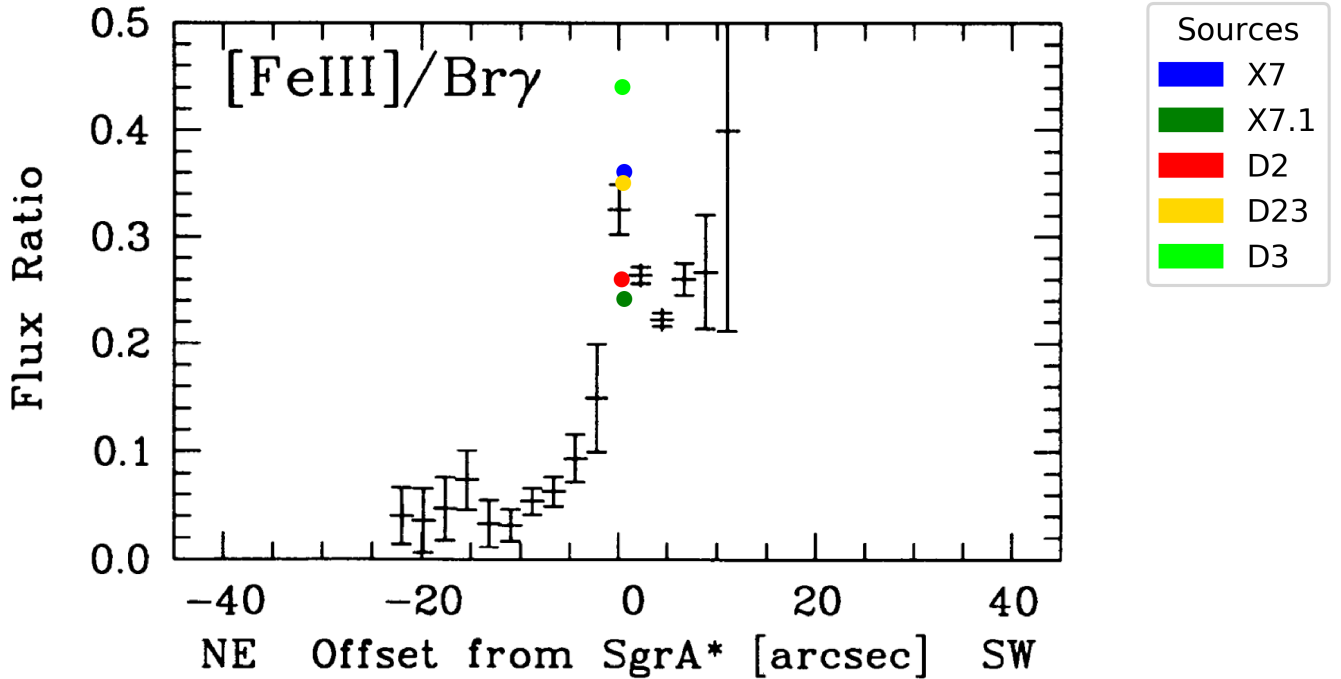


Fig. 10. [FeIII]/Bry flux ratio as a function of the Sgr A* offset. The plot is adapted from Lutz et al. (1993), the colored data points are extracted from the SINFONI data cube of 2015. We do not include X8 in this plot because its flux ratio is 0.67 and therefore outside the bonds of the adapted figure.

Table 9. Magnitudes of D2, D23 and D3 in the H -, K_S -, and L' -band in 2004 and 2015.

Source	mag $_H$	mag $_K$	mag $_{L'}$
D2	22.98	18.1 $^{+0.3}_{-0.8}$	13.5
D23	22.22	19.7 $^{+0.4}_{-0.3}$	15.13
D3	21.3	19.8	13.8

low-mass stars of $0.1\text{--}0.2 M_{\odot}$ move still vertically along the Hayashi track (Baraffe et al. 1998), being surrounded by accretion discs up to 10–20 Myr. D-objects could in principle manifest this “mass-separation” of young stars in the direct vicinity of Sgr A*, providing an opportunity for testing various star-formation models in the direct influence of the SMBH.

5. Discussion

Here we discuss our findings of the NACO and SINFONI analysis. We also give a brief outlook for upcoming observations and possibilities with the Mid-Infrared Instrument (MIRI).

5.1. NIR sources

Our analysis of the infrared H -, K -, and L' -data combined with the one- and two-component blackbody modeling shows that the dusty sources may be part of the S-cluster ($r < 0.04$ pc) population. These dusty sources are possible young stellar objects that are embedded in a potentially non-spherical dusty envelope as shown for the DSO/G2 (Fig. 12). These envelopes may include an optically thick dusty section, bipolar cavities, as well as a bow shock.

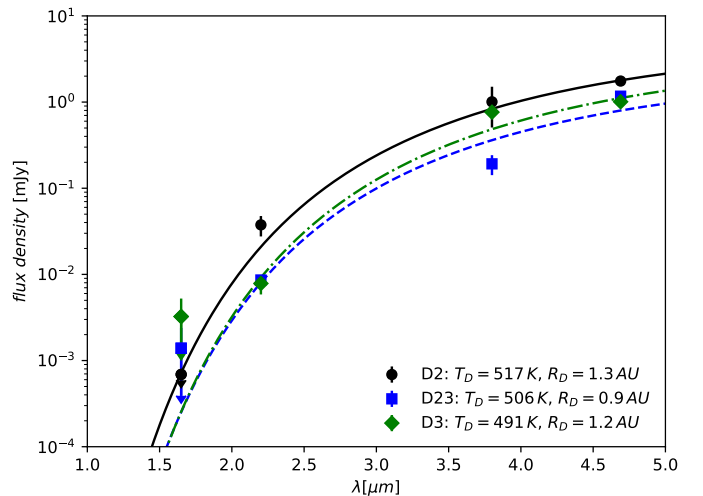


Fig. 11. Single-temperature blackbody models of three dusty sources – D2, D23, and D3 – are represented by lines (black-solid, blue-dashed, green-dashdot, respectively) with the parameters according to the legend. The continuum flux densities are depicted by points according to the legend.

Jalali et al. (2014) have focused particularly on the IRS 13N located 0.1 pc away from Sgr A*. Its properties suggest that these objects form a group of young stars with about five embedded young stellar objects (<1 Myr). Jalali et al. (2014) performed three-dimensional hydrodynamical simulations to follow the evolution of molecular clumps orbiting Sgr A*. Assuming that the molecular clumps are isothermal 50–100 K containing $100 M_{\odot}$ in a region of $\ll 0.2$ pc radius. Hence, the authors were able to constrain the formation and the physical conditions of such groups of young stars.

Table 10. Best-fit parameters (T_D , R_D) of the single-temperature BB model, including also the spectral slope (with the corresponding Lada YSO type), and the reduced χ^2 of the BB model.

Parameter	D2	D23	D3	DSO/G2 (1C-fit)	DSO/G2 (2C-fit)
T_D [K]	517 ± 10	506 ± 44	491 ± 40	626 ± 87	514 ± 41
R_D [AU]	1.26 ± 0.14	0.90 ± 0.39	1.17 ± 0.37	0.50 ± 0.31	0.97 ± 0.31
Slope KL' (Lada YSO class)	5.02 (I)	4.69 (I)	7.38 (I)	4.15 (I)	4.15 (I)
χ_r^2	1.51	11.12	5.76	6.20	1.00

Notes. The abbreviation 1C-fit stands for one component fit and 2C-fit represents two components – star and dusty envelope.

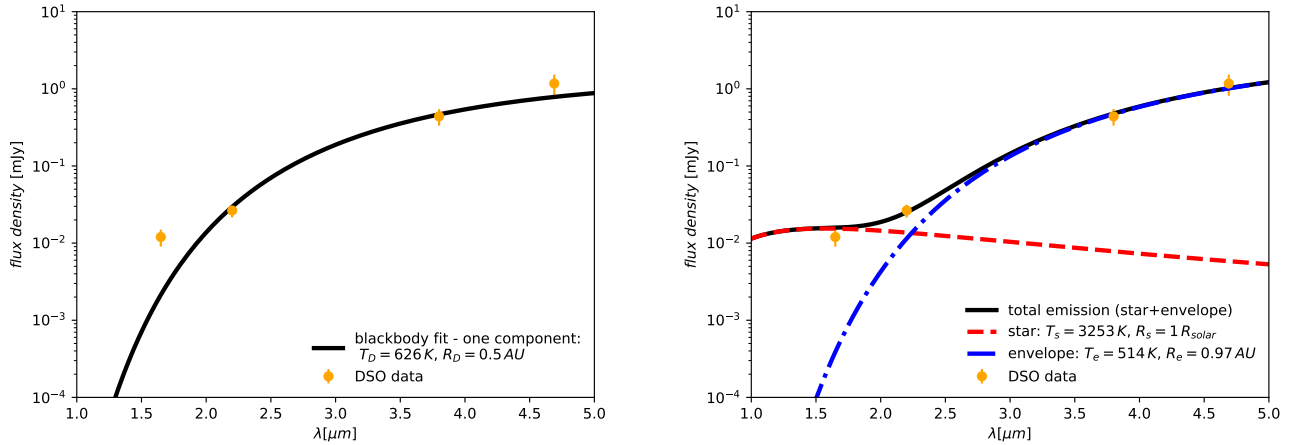


Fig. 12. Blackbody SED model of the DSO/G2 infrared source. *Left panel:* one component blackbody fit with the parameters according to the legend. Measured flux densities are depicted as orange points with corresponding errorbars. *Right panel:* two-component blackbody fit (star+dusty envelope). The black solid represents the total emission, while the red dashed line stands for the stellar emission and the blue dot-dashed line represents the dusty envelope emission with the parameters set according to the legend.

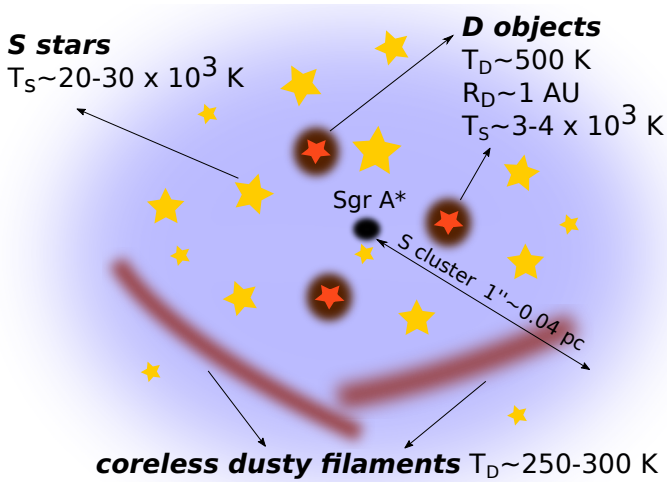


Fig. 13. Illustration of colder D-objects as dust-enshrouded stars inside the S cluster that consists predominantly of stars of spectral type B. D-objects have the characteristic temperature of ~ 500 K, which is larger than the temperature of other dusty structures in the region, namely the minispiral filaments of 200–300 K.

The authors also argue that such molecular clumps can originate in the CNB. Dissipation of orbital energy in the CNB result in highly eccentric orbits with clumps experiencing a strong compression along the orbital radius vector and perpendicular to the orbital plane. This causes increased gas densities higher than the tidal density of Sgr A*, triggering the rapid formation of solar mass stars.

5.1.1. D2, D23, D3, D3.1

In Fig. 2, we show dusty sources D2 and D3 with the newly discovered objects D23 and D3.1. In 2006, these sources were still isolated compared to 2015, where the chance of confusion is high.

Since there is an overlap of D3 and D3.1 (see Fig. 3), the shape of the spectrum shows multiple peaks. We identify the D3 related Doppler-shifted emission peaks with the SINFONI line maps. However, a bipolar morphology (Yusef-Zadeh et al. 2017a; Peißker et al. 2019), that is indicated by a complex peak structure, could be speculated and is discussed in Sect. 5.2. For the sake of completeness, it should be mentioned that the chance of confusion for the identification of D3.1 in the SINFONI data cubes is rather high in 2015. Spectroscopically, it is close to the Bry rest wavelength. However, we also find red-shifted HeI and [FeIII] emission lines at the approximate position of their related rest wavelength. Since the chosen location of the SINFONI FOV over various years does not cover the expected area of D3.1, we are not able to expand our analysis.

In contrast, the D-complex members D2, D23, D3 can be traced and analyzed as presented in Sect. 4. Based on our K - and L' -band data, we determine their magnitudes and give an upper limit for the H -band. Our single temperature BB model fits the flux emission of the dusty sources. In general, gas clouds or clumps in the vicinity of Sgr A* show temperatures much lower than our fitted model (see also Genzel et al. 2010). Therefore, the external heating of the dusty-sources seems unlikely. Vice versa, the dusty sources D2, D23, and D3 could have an internal heating source that might be indeed of stellar nature.

5.1.2. X7, X7.1, X8

The X-sources X7, X7.1, and X8 are grouped like the D-complex in the vicinity of Sgr A*. All three sources show Doppler-shifted HeI, Bry, and [FeIII] emission lines and can be detected in the SINFONI line maps. From the observations, it is not clear if X7 and X7.1 share a similar history because the detection of the latter one is limited to 2015. X7 can be detected in various bands with a comparable position angle (North-East) to X8 of around 45 deg. Because X7.1 is located too close to the edge of the SINFONI FOV, a analysis of the shape and its elongation is difficult. Since X7 and X8 show signs of a bow-shock (Mužić et al. 2010; Peißker et al. 2019), we can just speculate if X7.1 might also share a similar nature. This, however, could be part of future observation programs. If a bow-shock could be confirmed for X7.1, it might add another source to the proposed wind-direction of East-North to South-West with respect to Sgr A* (Yusef-Zadeh et al. 2012; Shahzamanian et al. 2015). This would increase the importance of the X-sources since the proper motion of at least X7 is directed in a direction, where no wind should be active. Therefore, X7 could change its shape in the future.

5.1.3. DSO, G1, D5, D9

Like the DSO/G2, G1 survived its peri-center passage without being disrupted and can be traced on a highly eccentric orbit (see Fig. 1 for a detection of G1 after the pericenter passage in 2008). As Witzel et al. (2017) and Zajaček et al. (2017) points out, these two sources are more likely a YSO or star embedded in a dusty envelope. This is underlined by the detection of the DSO/G2 source as a compact object at peri-apse by Witzel et al. (2014) as well as the *H*- and *K*-band detection presented and analyzed in this work (see Figs. F.1 and I.2). The, in several publications described, tidal evolution of the gas emission (Gillesen et al. 2013a,b; Pfuhl et al. 2015; Plewa et al. 2017) cannot be confirmed in our data-sets (see Valencia-S. et al. 2015). In contrast, we are detecting a compact source close to periapse in 2013 (Figs. 4 and F.1). We want to add that the authors of Valencia-S. et al. (2015) show the sensitive connection between the subtracted background and the extracted spectrum of the source. Considering the report of a drag force for the DSO/G2 by Gillesen et al. (2019), it would be interesting to investigate the effect of the background subtraction.

In the case of the DSO/G2, dust-dust scattering could be accounted for the observed emission (Zajaček et al. 2017). Even though G1 and the DSO/G2 share some similarities, Witzel et al. (2017) conclude that both sources are not part of a gas streamer in the way, that was proposed by Pfuhl et al. (2015). The authors propose, that the emission of the two sources is rather of non-stellar origin. Considering also the polarization results of Shahzamanian et al. (2016) for the DSO/G2, the observational evidence presented by the authors strongly favors an explanation that goes beyond a pure gas-cloud model.

Some sources are moving out of the available SINFONI FOV because of their proper motion. D5 (Fig. 1 and Eckart et al. 2013), for example, can be barely observed after 2008. More observations are needed to expand the analysis in order to evaluate the nature of the object. This can also be applied to D9 that is located north of S2.

5.2. The case of D3 and D3.1

Figures 1 and 2 both show the sources D3 and D3.1 in the 2006 NACO dataset and the 2015 SINFONI cubs. Over 10 years,

both sources moved with a very similar projected proper motion direction towards the north-east (see Table D.2 and Fig. 9). They show Doppler-shifted Bry, HeI, and [FeIII] emission that clearly distinguishes these sources against the background emission. As indicated by Fig. 3, the bright Bry emission line of both sources is present in the spectrum as a double peak that is blue and red-shifted. As shown by Yusef-Zadeh et al. (2017a), star formation in the form of Bipolar outflow sources is still ongoing close to the Galactic center. For D3 and D3.1, it can just be speculated if the observed properties indicate the presence of a bipolar scenario. Judging by our orbit overview presented in Fig. 9, the possibility for a common origin for both sources is rather low. Currently, they are not targeted by a possible wind that probably originates at the position of Sgr A* (see Lutz et al. 1993; Mužić et al. 2010; Yusef-Zadeh et al. 2012, 2017b; Peißker et al. 2019, for more information). If the wind coming from Sgr A* causes a shock or the elongated shape that we observe for X7 and X8, the objects D3 and D3.1 but also D2 are the perfect candidates to prove its existence. For that matter, the speculated shielding from the ionizing X-ray radiation could lead to disappearing [FeIII] emission lines when these sources cross the discussed Bry-bar (Fig. 6, see Sect. 5.4) in the Galactic center. However, an identification of these sources is affected by a high chance of confusion when they move towards the more crowded S-cluster. For a clear identification in the objects in the vicinity of Sgr A*, spectroscopic information is crucial. Because of their dust, mid-infrared observations (with, e.g., MIRI) combined with a spectroscopic analysis is crucial to get a deeper understanding of these sources.

5.3. [FeIII] emission

In contrast to the already indicated, but not further commented, line detection of ionized iron for D2 and D3 in Meyer et al. (2014), we report in addition to the blue-shifted Bry and HeI, a Doppler-shifted [FeIII] $^3G-^3H$ multiplet for the investigated sources (see Fig. 3 and Sect. 4). A confusion, as mentioned by Depoy & Pogge (1994), with other near-infrared emission lines can be expelled since the observed [FeIII] lines are Doppler-shifted and can be thereby distinguished from other lines. For the X7, X7.1, X8, D2, D23, and D3 sources, a Doppler-shifted [FeIII] line emission is detected in the SINFONI data cubes (Fig. 1, 3). We find also a weak Doppler-shifted [FeIII] emission at the position of D3.1 that distinguishes the source from the rest wavelength emission. When it comes to the charge transfer reaction of [FeII] and [FeIII], the authors of Lutz et al. (1993) discuss the ratio of the ionized iron lines with



As pointed out by the authors, because of the missing information about the efficiency of the charge transfer reaction, it is difficult to evaluate the importance of the [FeIII] line compared to the total iron budget. Even though the amount of the, in this work analyzed sources, is low for a statistical evaluation, the findings indicate, that the chance is rather high to detect Doppler-shifted [FeIII] lines in dusty sources west of Sgr A*. So far, none of the observed sources east of the Bry emission bar (Fig. 6) are showing signs of Doppler-shifted [FeIII] lines. Even without the efficiency information, this could be explained by the charge transfer radiation equation (Eq. (6)). It can be speculated, that the origin of these lines is most probably the strong X-ray radiation of Sgr A*. A possible wind that originates at the position of the SMBH produces a shock front in the ambient medium in the form of the observed Bry-bar feature (Fig. 6).

5.4. Bry emission bar

The ionized and Doppler-shifted iron lines reported here can be detected throughout almost all sources that are located west of the Bry-bar that is observed in the SINFONI line maps at $2.1661\ \mu\text{m}$ (see Fig. 6, middle) that spans from north to south with a projected distance to Sgr A* of $\sim 0''.08$ in 2006 and $\sim 0''.15$ in 2015. This structural detail of the inner parsec can be observed in every available SINFONI data-set. Keeping this finding in mind, we shortly want to summarize the analysis of features at the position of Sgr A* that could be connected to the Bry-bar and speculate about a possible connection to the recent publication of Murchikova et al. (2019).

Lutz et al. (1993) reported a [FeIII] bubble around Sgr A*. It is speculated that the emission originates either in stellar winds or a jet-driven outflow from Sgr A*. The authors also presented a V-shaped Doppler-shifted [FeIII] feature directed towards the mini-cavity with a bow-shock morphology (see Figs. 1 and 6) and a LOS velocity of around $40\ \text{km s}^{-1}$. The position angle of the emission with respect to Sgr A* is around 45° .

Following this, Yusef-Zadeh et al. (2012) reported a teardrop-shaped X-ray feature roughly at the position of Sgr A*. The authors speculated that it is probably produced by a synchrotron jet or shocked winds that are created by mass losing stars and seems to be consistent with the [FeIII] bubble shown in Lutz et al. (1993). The ram pressure of the winds could then push the ionized bar away and produce the teardrop-shaped X-ray feature. However, the VLA data show that the bright X-ray feature is open towards the western side. It is unclear if this open side of the teardrop can be linked to the Bry-bar shown in Fig. 6.

If future observations of the Bry-bar could confirm a connection between [FeIII] bubble and the teardrop-shaped X-ray feature, it might indicate the transition of a region that is dominated by a strong wind to a region with a strong ionizing X-ray emission. This could explain the Doppler-shifted and ionized [FeIII] $^3G-^3H$ multiplet that can be observed in almost every dusty source west of the Bry transition feature (see Figs. 3 and 6). Recently, Murchikova et al. (2019) reported a blue- and red-shifted H30 α emission around Sgr A* with a line width of over $2000\ \text{km s}^{-1}$ on scales that are comparable to the here presented SINFONI data. Based on the presented data of the authors, there is a small but noticeable gap of the Doppler-shifted H30 α feature. The authors report a displacement of the red-shifted H30 α side of around 0.11 as or 110 mas. Based on our SINFONI data-cube, the Bry-bar reported here shows a measured size of 0.10–0.12 as and could, therefore, be connected to the reported Doppler-shifted H30 α feature by Murchikova et al. (2019).

5.5. [FeIII] distribution in the Galactic center around Sgr A*

We have already discussed the [FeIII]-bubble analyzed by Lutz et al. (1993). In addition, we aim to draw a connection between the large scale [FeIII] distribution from the same publication (see Fig. 1) that is located south-east of Sgr A* at a distance of a few arcsec. This distribution is arranged in a V-shape and at the position of the mini-cavity. The IRS13 complex can also be found inside of this bow-shock like feature that contains many dusty sources with iron emission lines (Mužić et al. 2008). We show in Fig. 1 that the iron distribution is in close contact to the position of Sgr A*. As mentioned before, it is plausible, that iron in the Galactic center is not only created by a continuous distribution, but also by compact sources as, for example, IRS13N (Mužić et al. 2008) or the D-complex (this work). Based on our spectral

analysis, we speculate that the chance of finding dusty sources with iron emission lines is higher inside the V-shaped [FeIII] feature compared to dusty sources outside of the iron distribution. We discussed, that the detection of the here discussed sources can be divided by the bright and prominent Bry-bar (Figs. 1 and 6).

As mentioned before, Eckart et al. (1992), Lutz et al. (1993), and Yusef-Zadeh et al. (2017a) report a bubble of hot gas that is found around Sgr A*. It is still unclear why the bubble around Sgr A* is open towards the western direction. It may be speculated that perhaps the S-stars or the Bry-bar reported here are shielding the dust grains against depletion of [FeIII] (Jones (2000), Zhukovska et al. 2018), which leads to the presence of large amounts of excited iron in the gas phase. At the transition edge (Figs. 1 and 6), hydrogen gets excited and the depletion of [FeIII] from the dust grains of the dusty sources is increased. Upcoming observations with MIRI and long term monitoring with SINFONI on larger scales of these sources and the GC will probably reveal more interesting details about the connection of the Sgr A* bubble, the wind, the Doppler-shifted H30 α emission presented in Murchikova et al. (2019), and the presented north- to south Bry-bar. These observations are becoming more important for the future since some dusty sources, such as D2 and D3, are moving in projection towards regions where no wind features are present. We expect that the Doppler-shifted [FeIII] emission lines could be dampened or vanish completely. This is also reflected in Fig. 10. Partially, this plot is adapted from Lutz et al. (1993) and complemented with our measurements. The plot suggests that a possible ionization wind shows an increased impact towards Sgr A* from the north-eastern direction. This trend continues towards south-west till the V-shaped bow shock-like feature at the position of the mini-cavity (Figs. 1 and 6).

5.6. Indications from the [FeIII] findings

5.6.1. Iron distribution in the GC

We assume the dust-growth ratios presented in Zhukovska et al. (2018), where the authors discuss the spallation of iron from dust grains into the gas-phase. Combined with the LOS, our results (Fig. 10) are in agreement with the presented connection in Jones (2000) between shock velocity and dust-depletion of Fe. The [FeIII] flux presented in Fig. 10 originates in the mini-cavity (black data points) and could be associated with an ionized V-shaped structure that shows a bow-shock morphology (Lutz et al. 1993; Yusef-Zadeh et al. 2012). The detection of compacted sources close to Sgr A* could indicate that the [FeIII] distribution in the mini-cavity could be influenced strongly by single dusty-sources (this work; Moultaqa et al. 2006; Mužić et al. 2008).

5.6.2. Iron as an indication for YSOs

As mentioned in Sect. 5.3, we want to discuss the significance of the Doppler-shifted [FeIII] emission line compared to the total iron budget. As shown by Depoy (1992), the derived [FeII]/Bry ratio is between 0.5 ($5''$ south of IRS7) and 0.7 ($10''$ south of IRS7). IRS7 is located around $5''.5$ north of Sgr A*. Therefore, it is reasonable to assume, that a ratio of around 0.55 ± 0.1 is in good agreement with the derived values. Taking into account our measurements (Table 8 and Fig. 10), we find an averaged value for the amount of [FeIII] to [FeII] of around 0.7. This naive approach does not take different densities or temperatures into account. However, Lutz et al. (1993) derive, using values from

Depoy (1992) for the $[\text{FeII}]/[\text{FeI}]$ ratio, a result of ≈ 1 in the GC. Additionally, our averaged AIP value of 0.38 is in excellent agreement with the commonly derived $[\text{FeIII}]/\text{Br}\gamma$ ratios (Depoy 1992; Lutz et al. 1993; Luck et al. 1998). Therefore, the presence of the detected $[\text{FeIII}]$ emission line of the sources could be used as an indicator for the metallicity (Kamath et al. 2014) or at least for the high abundance in metals. Moreover, it emphasizes the dusty nature of the objects (Zhukovska et al. 2018). Oliveira et al. (2013), Shimonishi et al. (2016), and, most recently, Sciortino et al. (2019) underline in their studies iron and metallicity as an important star formation parameter. The hypothesis that the nature of the dusty sources can be described as recently formed YSOs (Yusef-Zadeh et al. 2017a; Zajaček et al. 2017) becomes, therefore, more permissible. This is briefly summarized in the following.

5.7. Origin of the NIR excess sources

When it comes to the origin of the Doppler-shifted $\text{Br}\gamma$ sources that surround Sgr A* on highly eccentric orbits, which we discuss here, we speculate that they are stellar in nature. We associate them with dust-enshrouded stars that may, in fact, could have been formed very recently through the mechanism put forward by Jalali et al. (2014). These mechanisms are also part of the discussion presented by Tsuboi et al. (2016) and Trani et al. (2016). Based on the fact that D2, D23, and D3 show the same spectral features and have similar magnitudes, it seems to be plausible that they are part of one population when we consider the aforementioned publication. They might be dust-embedded pre-main-sequence stars presumably forming a small bow shock (Shahzamanian et al. 2016; Zajaček et al. 2017). Yoshikawa et al. (2013), Yusef-Zadeh et al. (2017b), and Naoz et al. (2018) discuss and show several plausible scenarios that underline the presence of binaries, YSOs, and intrinsically polarized low-mass stars, as well as bow-shock sources in the GC close to Sgr A*.

In addition, Mužić et al. (2007, 2008) present trajectories of dusty sources that are comoving in groups. This is already separately analyzed in Eckart et al. (2013), where the authors discuss that randomly located dusty sources in the GC can be found with a likelihood of around 25% per resolution element and observing epoch. They derive, that comoving objects in the GC can be observed with a probability of several percents. These two observational and statistical findings can be directly applied to the found sources D2, D23, D3, D3.1, X8, X7, and X7.1. These sources are either comoving (see Fig. 9) or can be found in groups (see Fig. 2).

If upcoming observations could confirm the proposed nature of the sources given in this work, the identification of the $[\text{FeIII}]$ multiplet in unknown dusty sources could be used to underline their stellar character. However, the DSO/G2 spectrum does not show any signs of a $[\text{FeIII}]$ line. But as shown in Fig. 12, the presented SED model based on our H - and K -band detection (Fig. F.1) fits a stellar core with a dusty envelope.

5.8. Upcoming opportunities with MIRI

Here we want to discuss the impact of the mid-infrared instrument MIRI of the *James Webb Space Telescope* (see Bouchet et al. 2015; Ressler et al. 2015; Rieke et al. 2015, for further information). Compared to the presented data in this work, MIRI will operate in the M -band. This will allow us to observe the here discussed sources with higher precision because of a more stable PSF. Since the SINFONI introduces an elongated PSF with changing x - and y -values for the FWHM, an optimized PSF

for the high-pass filtering is necessary. The wings of close-by sources do interact in a way, that artificial signals could be created (Sabha et al. 2012; Eckart et al. 2013). Additionally, sky emission lines can have an unavoidable influence on the spectrum that is described in Davies (2007). Hence, the investigation of dusty sources with MIRI in the central stellar cluster will greatly benefit from the up-cumming improved observational possibilities. Foremost, we have the JWST instrumentation that will allow us to obtain sensitive spectroscopy without the mentioned atmospheric and instrumental effects of individual sources in this densely populated region. In particular, the IFU observations with MIRI will be helpful to obtain broadband spectroscopy covering a few to several 10 micrometers. While spatial deconvolution of the resulting data cubes at longer wavelengths will be essential, the sources should readily be separable at the short-wavelength end of the spectrometers. The highest angular resolution and diagnostic spectral line tracers available in MIRI are essential to making further progress in this investigation of the dusty sources; especially when it comes to the local and general line of sight ISM towards them through ice absorption features, for example, H_2O , CH_4 , CO , NH_3 . Also, emission features from gaseous molecules like H_2 , CO , H_2O , CH_4 , C_2H_2 , HCN , OH , SiO could provide a new insight of the nature and origin of the observed objects. Some of these emission lines like CH_4 , C_2H_2 that can be found in gas and ice can be used as probes for stellar disks. For the Galactic Center, we have already shown in Moultaqa et al. (2006, 2009) the importance of the H_2O line emission and the CO gas and ice absorption to study the extinction towards the Galactic Center and the properties of the GC interstellar medium.

6. Summary and Conclusions

We present a detailed analysis of two of the dusty NIR excess sources within the central arcseconds of the Galactic Nucleus, close to the supermassive black hole Sgr A*. These dust sources are of special interest as their existence had not been predicted and may be indicative for ongoing star formation in this complex region.

6.1. Properties of the NIR excess sources

We successfully fitted Keplerian orbits to both sources, D2 and D3. Furthermore, we found new sources that we named D23 and D3.1. D2, D3, and D3.1 have an elliptical orbit with similar orbital parameters. They also show Doppler-shifted $\text{Br}\gamma$, HeI and $[\text{FeIII}]$ line emission exhibiting comparable line-of-sight velocities indicating that they arise from the same source. Both, the $\text{Br}\gamma$ and $[\text{FeIII}]$ line emission, occur from high excitation shocked regions (see e.g., Tielens et al. 1994; Zhukovska et al. 2018). Since D23 shows a clockwise orbital trajectory, this D-source might be part of other, not discovered groups of dusty emission objects.

The obtained K_S -band magnitudes are $18.1^{+0.3}_{-0.8}$ for D2 and $19.7^{+0.4}_{-0.3}$ for D3. In the H -band, we derived upper limits to their magnitudes of 22.98 for D2 and 22.22 for D3, respectively. Valencia-S. et al. (2015) and Zajaček et al. (2017) show that for a $1\text{--}2 M_\odot$ embedded pre-main-sequence star, hot accretion streams of matter very close to the star can fully account for its observed $\text{Br}\gamma$ luminous in combination with the line widths covering a range from 200 km s^{-1} to 700 km s^{-1} . These streams can possibly exist in combination with disk winds. As indicated by pre-main-sequence evolutionary tracks of low- and

intermediate-mass stars (see, e.g., [Siess et al. 2000](#)) it is entirely conceivable that after an initial phase of less than 10^6 years the $1\text{--}2 M_{\odot}$ stars present themselves in a T Tauri stage with a luminosity that does not exceed $10 M_{\odot}$ (see also [Chen et al. 2014](#)).

Comparing the derived flux values for the DSO/G2 with a two component blackbody model and detecting the object in the H - and K -band continuum shows that the source might be indeed a pre-main-sequence star embedded in a dusty envelope as already discussed by [Shahzamanian et al. \(2016\)](#) and [Zajaček et al. \(2017\)](#). We successfully fitted also a single component BB model to the observed emission of D2, D23, and D3. Since the gas temperatures in the vicinity do not exceed 50 K–200 K ([Genzel et al. 2010](#)), it is obvious that a simple gas-cloud nature of the sources can be excluded. In combination with their Keplerian orbital motion, we see a strong tendency towards a stellar scenario. This is also supported by the H -band detection of the DSO/G2, which clearly favors the combined star+envelope model over the pure core-less cloud model. Young stellar objects of type I ([Lada et al. 1987](#)) could be a plausible explanation. Adjustment of several variables, such as the accretion rate of the YSOs, the viewing angle, and the dust temperature, might improve the SED of the near-infrared and mid-infrared fluxes. The intrinsic colors are consistent with a dust temperature of 500 K. The surrounding shell or disk, as well as the accretion material, can provide enough extinction to explain the observed infrared colors ([Eckart et al. 2013](#)).

6.2. Linkage to flaring activity

The data obtained for the DSO are consistent with a very compact source on an elliptical orbit. It is sufficiently compact that it has not influenced the flaring activity of the black hole in any statistically convincing way. That does however not exclude the possibility that an increase in accretion activity of Sgr A* may still be upcoming. However, the crossing time scales for the region in which the DSO passed by Sgr A* is only a few years, even if one includes effects from a possible wind from Sgr A*. Any Sgr A* activity occurring at times more than a few years from now become increasingly more difficult to be associated with the DSO passage close to Sgr A* when one considers in-spiral time scales of several decades. Distinguishing between the DSO/G2 passage and for example, the G1 source might be challenging. Both sources passed Sgr A* at a comparatively distance at $a_{\min} = 200\text{--}300$ a.u. ([Witzel et al. 2017](#)). As discussed, it becomes increasingly likely that the dust embedded sources are associated rather with young accreting stars than core-less gas and dust clouds. An identification of the DSO, D2, D23, and D3 with a dust embedded stars also puts the necessity of a common history of the DSO and G1 source at risk ([Pfuhl et al. 2015](#)). Due to the higher mass ($\sim 1\text{--}2 M_{\odot}$), the action of drag forces on these objects is also more than questionable ([Gillissen et al. 2019](#)).

6.3. Bow shock stars

The Bry and [FeIII] lines detected here might arise from collisional excitation in the inner bow shock. Also, accretion processes onto a central star is an option that can be considered. Furthermore, it is presumed that the Bry emission lines originate in photoionization of a UV radiation field. [FeIII] emission requires a high iron abundance gas, which can be created in shocks. The high abundance gas then has to be ionized, either by UV photons or by collisions.

A possible bow shock might either be caused by strong stellar winds coming from, for example, IRS13 or by an outflow from the Galactic Center. Moreover, the bow shock could arise from the potential supersonic motion of D2 and D3.

[Shahzamanian et al. \(2016\)](#) and [Zajaček et al. \(2017\)](#) constrain the nature and the geometry of the DSO. The authors compare 3D radiative transfer models of the DSO with the near-infrared (NIR) continuum data including NIR K -band polarimetry. They present a composite model of the DSO with a dust-enshrouded star that consists of a stellar source, dusty, optically thick envelope, bipolar cavities, and a bow shock.

6.4. An alternative to the thermal young stellar object model

An alternative scheme can explain the continuum emission via the non-thermal contribution of young neutron stars and their wind nebulae ([Zajaček et al. 2014, 2017](#)). Their proposed model can match the NIR fluxes as well as polarized properties of the observed spectral energy distribution. The authors also show that, in principle, the SED may be explained by a young pulsar wind nebula (PWN). However, the analysis of the neutron star model shows that young, energetic neutron stars should be detected as near-infrared-excess sources which also exhibit themselves by the magnetospheric synchrotron emission. Both the thermal and the non-thermal models are thus consistent with the observed properties of these sources, that is, their compactness, the total and (for the DSO) the polarized continuum emission. Nevertheless, there are as yet no such detections of X-ray and radio counterparts of the dusty sources.

[Naoz et al. \(2018\)](#) discuss the possibility that binaries could play a major role by contributing and explaining observed properties of the GC disk. With that, the number of similar objects, as discussed here, could be much higher but also expected. The LOS velocities of the investigated objects are consistent with the discussed binary velocities v_z as a function of the semi-major axis of the GC disk.

Recently, [Yusef-Zadeh et al. \(2017b\)](#) reported the detection of bipolar outflow sources with ALMA. The authors find evidence for low-mass star formation even though considering the difficulties, distinguishing between low-mass YSOs from starless dusty cores ([Gillissen et al. 2012](#); [Eckart et al. 2013](#)). However, the findings of [Yusef-Zadeh et al. \(2017b\)](#) are in line with [Yoshikawa et al. \(2013\)](#), where the authors report that intrinsically polarized stars could be associated with YSOs. At least for the DSO/G2, [Shahzamanian et al. \(2016\)](#) finds a polarization degree of $>20\%$. A future polarization analysis of the remaining here discussed sources could contribute to a more detailed discussion about the nature of the dusty-sources in the GC.

Acknowledgements. This work was supported in part by the Deutsche Forschungsgemeinschaft (DFG) via the Cologne Bonn Graduate School (BCGS), the Max Planck Society through the International Max Planck Research School (IMPRS) for Astronomy and Astrophysics, as well as special funds through the University of Cologne and SFB 956 – Conditions and Impact of Star Formation. Part of this work was supported by fruitful discussions with members of the European Union funded COST Action MP0905: Black Holes in a Violent Universe and the Czech Science Foundation – DFG collaboration (No. 19-01137J). MZ acknowledges the support by the National Science Centre in Poland (Maestro 9 grant No. 2017/26/A/ST9/00756). A. Eckart and V. Karas are grateful for support through the German Research Foundation (DFG) program E 137/10-1 and the Czech Science Foundation. We also would like to thank the members of the SINFONI/NACO and ESO’s Paranal/Chile team for their support and collaboration.

References

- Alig, C., Schartmann, M., Burkert, A., & Dolag, K. 2013, *Proc. Int. Astron. Union*, 9, 185
- Baraffe, I., Chabrier, G., Allard, F., & Hauschildt, P. H. 1998, *A&A*, 337, 403
- Barvainis, R. 1987, *ApJ*, 320, 537
- Bonnet, H., Abuter, R., Baker, A., et al. 2004, *The Messenger*, 117, 17
- Bouchet, P., García-Marín, M., Lagage, P.-O., et al. 2015, *Publ. Astron. Soc. Pac.*, 127, 612
- Briceño, C., Preibisch, T., Sherry, W. H., et al. 2007, in *Protostars and Planets V*, eds. B. Reipurth, D. Jewitt, & K. Keil, 345
- Burkert, A., Schartmann, M., Alig, C., et al. 2012, *ApJ*, 750, 58
- Calderón, D., Cuadra, J., Schartmann, M., et al. 2018, *MNRAS*, 478, 3494
- Chen, Y., Girardi, L., Bressan, A., et al. 2014, *MNRAS*, 444, 2525
- Ciurlo, A., Campbell, R. D., Morris, M. R., et al. 2020, *Nature*, 577, 337
- Clénet, Y., Rouan, D., Gendron, E., et al. 2001, *A&A*, 376, 124
- Clénet, Y., Rouan, D., Lacombe, F., Gendron, E., & Gratadour, D. 2003, *Astron. Nachr. Suppl.*, 324, 327
- Clénet, Y., Rouan, D., Gratadour, D., et al. 2005, *A&A*, 439, L9
- Cotera, A., Morris, M., Ghez, A. M., et al. 1999, in *The Central Parsecs of the Galaxy*, eds. H. Falcke, A. Cotera, W. J. Duschl, F. Melia, & M. J. Rieke, *ASP Conf. Ser.*, 186, 240
- Davies, R. I. 2007, *MNRAS*, 375, 1099
- Depoy, D. L. 1992, *ApJ*, 398, 512
- Depoy, D. L., & Pogge, R. W. 1994, *ApJ*, 433, 725
- Dodds-Eden, K., Gillessen, S., Fritz, T. K., et al. 2011, *ApJ*, 728, 37
- Eckart, A., & Genzel, R. 1996, *ASP Conf. Ser.*, 102, 196
- Eckart, A., Genzel, R., Krabbe, A., et al. 1992, *Nature*, 355, 526
- Ghez, A. M., Mužić, K., Yazici, S., et al. 2013, *A&A*, 551, A18
- Eckart, A., Hüttemann, A., Kiefer, C., et al. 2017, *Found. Phys.*, 47, 553
- Eisenhauer, F., Abuter, R., Bickert, K., et al. 2003, in *Instrument Design and Performance for Optical/Infrared Ground-based Telescopes*, eds. M. Iye, & A. F. M. Moorwood, *Proc. SPIE*, 4841, 1548
- Eisenhauer, F., Genzel, R., Alexander, T., et al. 2005, *ApJ*, 628, 246
- Fritz, T. K., Gillessen, S., Dodds-Eden, K., et al. 2011, *ApJ*, 737, 73
- Genzel, R., Eisenhauer, F., & Gillessen, S. 2010, *Rev. Mod. Phys.*, 82, 3121
- Ghez, A. M., Klein, B. L., Morris, M., & Becklin, E. E. 1998, *ApJ*, 509, 678
- Ghez, A. M., Duchêne, G., Matthews, K., et al. 2003, *ApJ*, 586, L127
- Gillessen, S., Eisenhauer, F., Trippe, S., et al. 2009, *ApJ*, 692, 1075
- Gillessen, S., Genzel, R., Fritz, T. K., et al. 2012, *Nature*, 481, 51
- Gillessen, S., Genzel, R., Fritz, T. K., et al. 2013a, *ApJ*, 774, 44
- Gillessen, S., Genzel, R., Fritz, T. K., et al. 2013b, *ApJ*, 774, 44
- Gillessen, S., Plewa, P. M., Widmann, F., et al. 2019, *ApJ*, 871, 126
- Gravity Collaboration (Abuter, R., et al.) 2018, *A&A*, 615, L15
- Gravity Collaboration (Abuter, R., et al.) 2019, *A&A*, 625, L10
- Habibi, M., Gillessen, S., Martins, F., et al. 2017, *ApJ*, 847, 120
- Jalali, B., Pelupessy, F. I., Eckart, A., et al. 2014, *MNRAS*, 444, 1205
- Jones, A. P. 2000, *J. Geophys. Res.*, 105, 10257
- Kamath, D., Wood, P. R., & Van Winckel, H. 2014, *MNRAS*, 439, 2211
- Lada, C. J. 1987, in *Star Forming Regions*, eds. M. Peimbert, & J. Jugaku, *IAU Symp.*, 115, 1
- Lenzen, R., Hartung, M., Brandner, W., et al. 2003, in *Instrument Design and Performance for Optical/Infrared Ground-based Telescopes*, eds. M. Iye, & A. F. M. Moorwood, *Proc. SPIE*, 4841, 944
- Levin, Y., & Beloborodov, A. M. 2003, *ApJ*, 590, L33
- Luck, R. E., Moffett, T. J., Barnes, T. G., & Gieren, W. P. 1998, *AJ*, 115, 605
- Lucy, L. B. 1974, *AJ*, 79, 745
- Lutz, D., Krabbe, A., & Genzel, R. 1993, *ApJ*, 418, 244
- Meyer, F., & Meyer-Hofmeister, E. 2012, *A&A*, 546, L2
- Meyer, L., Ghez, A. M., Witzel, G., et al. 2014, *IAU Symp.*, 303, 264
- Modigliani, A., Hummel, W., Abuter, R., et al. 2007, *ArXiv e-prints* [arXiv:astro-ph/0701297]
- Morris, M., & Serabyn, E. 1996, *ARA&A*, 34, 645
- Moultaka, J., Eckart, A., Viehmann, T., & del Schö, R. 2006, in *Journal of Physics Conference Series*, eds. R. del Schö, G. C. Bower, M. P. Muno, S. Nayakshin, & T. Ott, 54, 57
- Moultaka, J., Eckart, A., & Schödel, R. 2009, *ApJ*, 703, 1635
- Murchikova, E. M., Phinney, E. S., Pancoast, A., & Blandford, R. D. 2019, *Nature*, 570, 83
- Mužić, K., Eckart, A., Schödel, R., Meyer, L., & Zensus, A. 2007, *A&A*, 469, 993
- Mužić, K., Schödel, R., Eckart, A., Meyer, L., & Zensus, A. 2008, *A&A*, 482, 173
- Mužić, K., Eckart, A., Schödel, R., et al. 2010, *A&A*, 521, A13
- Naoz, S., Ghez, A. M., Hees, A., et al. 2018, *ApJ*, 853, L24
- Oliveira, J. M., van Loon, J. T., Sloan, G. C., et al. 2013, *MNRAS*, 428, 3001
- Parsa, M., Eckart, A., Shahzamanian, B., et al. 2017, *ApJ*, 845, 22
- Peißker, F., Zajaček, M., Eckart, A., et al. 2019, *A&A*, 624, A97
- Pfuhl, O., Gillessen, S., Eisenhauer, F., et al. 2015, *ApJ*, 798, 111
- Plewa, P. M., Gillessen, S., Eisenhauer, F., et al. 2015, *MNRAS*, 453, 3234
- Plewa, P. M., Gillessen, S., Pfuhl, O., et al. 2017, *ApJ*, 840, 50
- Pych, W. 2004, *PASP*, 116, 148
- Ressler, M. E., Sukhatme, K. G., Franklin, B. R., et al. 2015, *Publ. Astron. Soc. Pac.*, 127, 675
- Rieke, G. H., Wright, G. S., Böker, T., et al. 2015, *Publ. Astron. Soc. Pac.*, 127, 584
- Rousset, G., Lacombe, F., Puget, P., et al. 2003, in *Adaptive Optical System Technologies II*, eds. P. L. Wizinowich, & D. Bonaccini, *Proc. SPIE*, 4839, 140
- Sabha, N., Eckart, A., Merritt, D., et al. 2012, *A&A*, 545, A70
- Schartmann, M., Burkert, A., Alig, C., et al. 2012, *ApJ*, 755, 155
- Schödel, R., Najarro, F., Muzic, K., & Eckart, A. 2010, *A&A*, 511, A18
- Schödel, R., Ott, T., Genzel, R., et al. 2002, *Nature*, 419, 694
- Sciortino, S., Flaccomio, E., Pillitteri, I., & Reale, F. 2019, *Astron. Nachr.*, 340, 334
- Scoville, N., & Burkert, A. 2013, *ApJ*, 768, 108
- Shahzamanian, B., Eckart, A., Valencia-S., M., et al. 2015, *The Messenger*, 159, 41
- Shahzamanian, B., Eckart, A., Zajaček, M., et al. 2016, *A&A*, 593, A131
- Shimonishi, T., Onaka, T., Kawamura, A., & Aikawa, Y. 2016, *ApJ*, 827, 72
- Siess, L., Dufour, E., & Forestini, M. 2000, *A&A*, 358, 593
- Tielens, A. G. G. M., McKee, C. F., Seab, C. G., & Hollenbach, D. J. 1994, *ApJ*, 431, 321
- Tokunaga, A. T., & Vacca, W. D. 2007, in *The Future of Photometric, Spectrophotometric and Polarimetric Standardization*, ed. C. Sterken, *ASP Conf. Ser.*, 364, 409
- Trani, A. A., Mapelli, M., Bressan, A., et al. 2016, *ApJ*, 818, 29
- Tsuboi, M., Kitamura, Y., Uehara, K., Miyawaki, R., & Miyazaki, A. 2016, *Proc. Int. Astron. Union*, 11, 115
- Valencia-S., M., Eckart, A., Zajaček, M., et al. 2015, *ApJ*, 800, 125
- Witzel, G., Eckart, A., Bremer, M., et al. 2012, *ApJS*, 203, 18
- Witzel, G., Ghez, A. M., Morris, M. R., et al. 2014, *ApJ*, 796, L8
- Witzel, G., Sitariski, B. N., Ghez, A. M., et al. 2017, *ApJ*, 847, 80
- Wollman, E. R., Geballe, T. R., Lacy, J. H., Townes, C. H., & Rank, D. M. 1977, *ApJ*, 218, L103
- Yoshikawa, T., Nishiyama, S., Tamura, M., Ishii, M., & Nagata, T. 2013, *ApJ*, 778, 92
- Yusef-Zadeh, F., Arendt, R., Bushouse, H., et al. 2012, *ApJ*, 758, L11
- Yusef-Zadeh, F., Wardle, M., Kunneriath, D., et al. 2017a, *ApJ*, 850, L30
- Yusef-Zadeh, F., Schödel, R., Wardle, M., et al. 2017b, *MNRAS*, 470, 4209
- Zajaček, M., Karas, V., & Eckart, A. 2014, *A&A*, 565, A17
- Zajaček, M., Britzen, S., Eckart, A., et al. 2017, *A&A*, 602, A121
- Zhukovska, S., Henning, T., & Dobbs, C. 2018, *ApJ*, 857, 94

Appendix A: Complementary orbit plots of the dusty sources

A.1. Orbit plot of D23 and D31

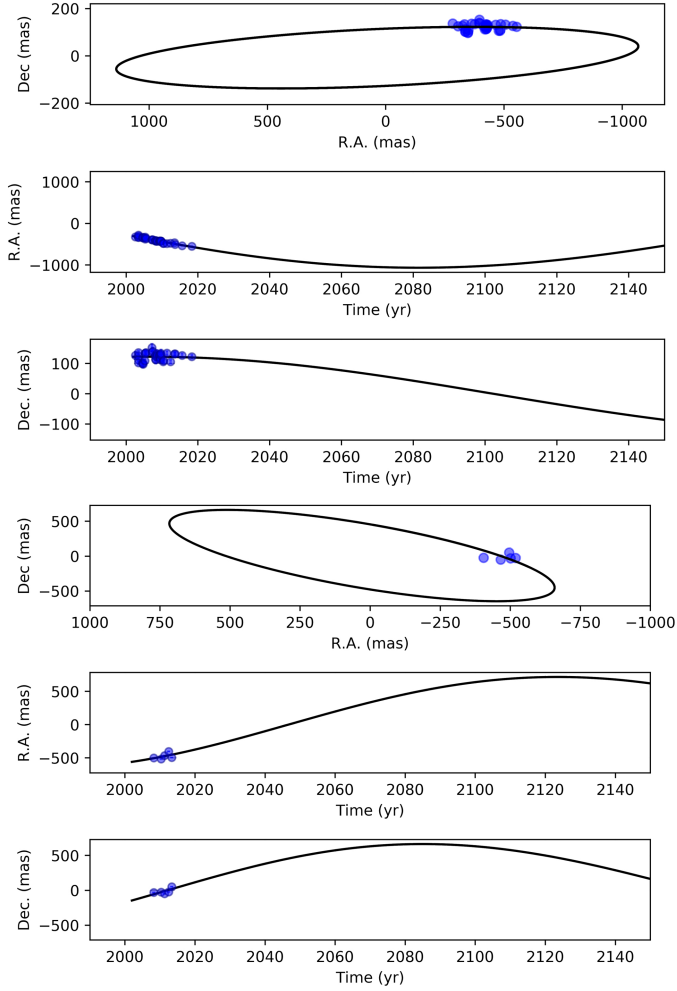


Fig. A.1. Orbit overview of D23 and D31. *Upper plot:* D23-, *lower plot:* D31-orbit. The data is based on the Keplerian fit presented in Tables D.1 and D.2.

A.2. Velocity plots of D2 and D3

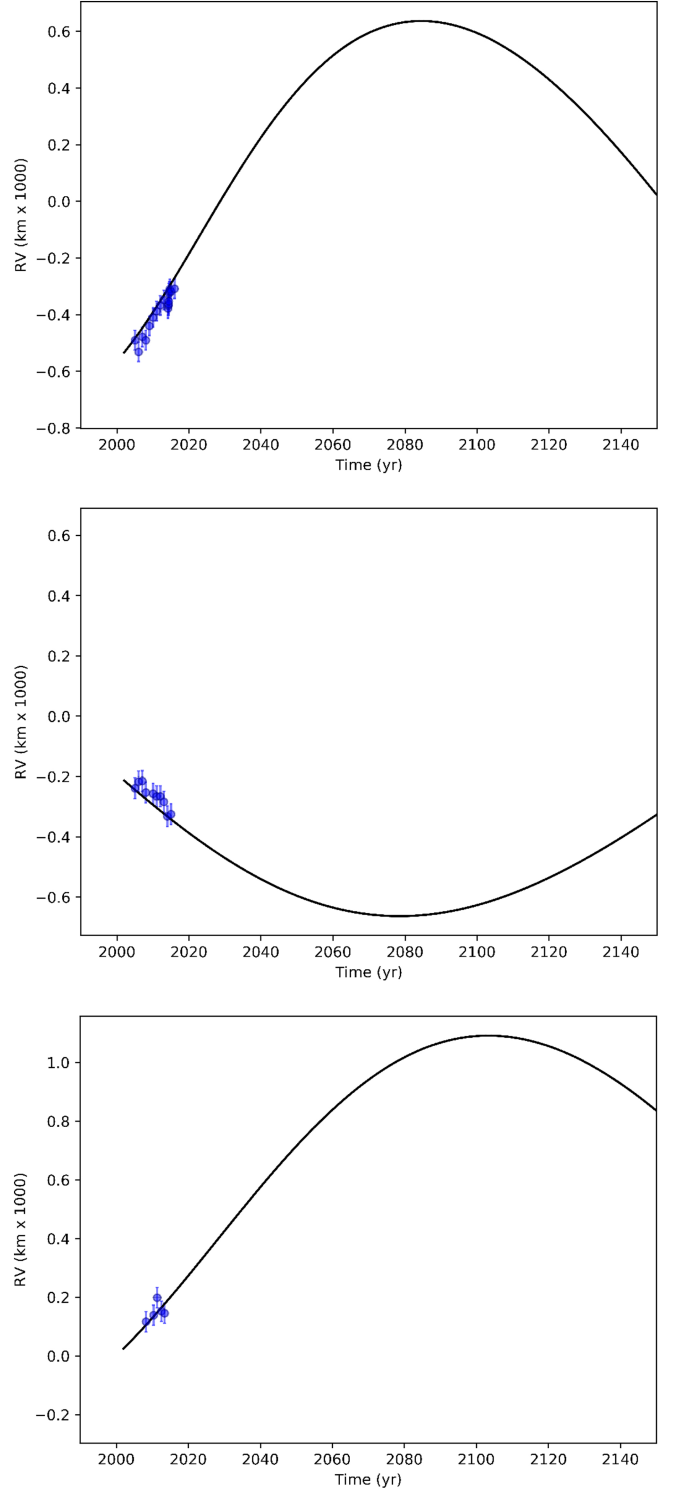


Fig. A.2. Line-of-sight velocity fit of D2, D23, and D31. *Upper plot:* LOS fit of D2, *middle plot:* related to D23, and *lower plot:* D3.1 fit. The data is extracted from the SINFONI data-cubes. Because the minimal amount of data for D3, the fit shows a poor response.

A.3. AIP ratio of the dusty sources

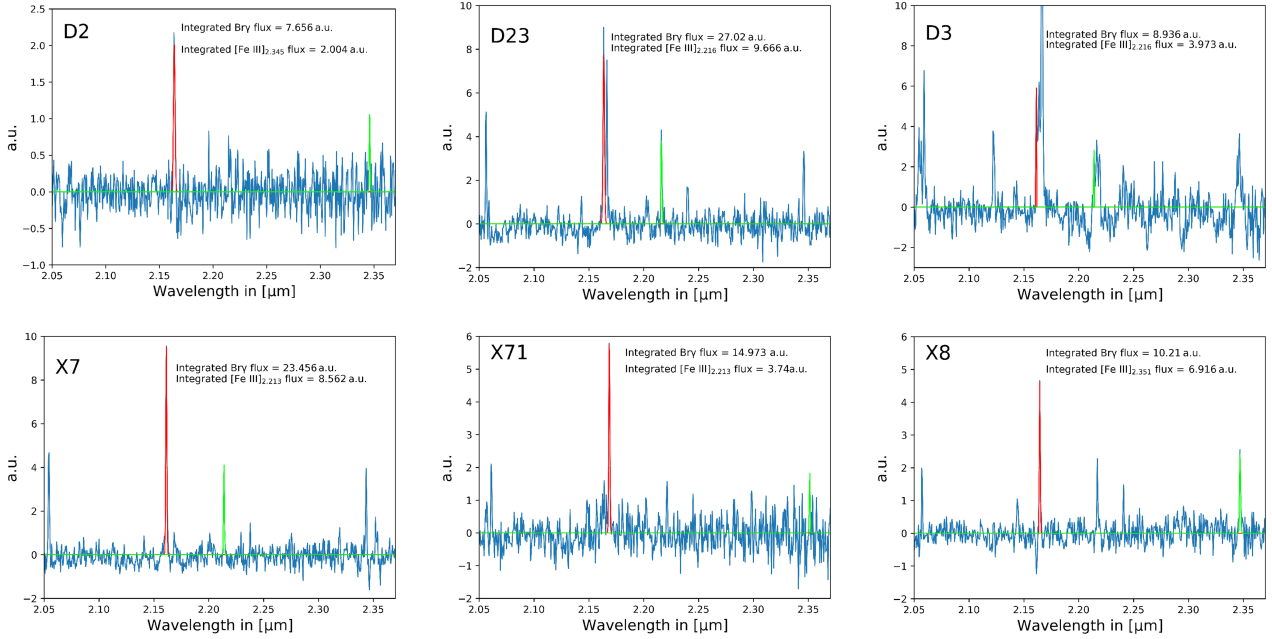


Fig. A.3. Gaussian fit of the Doppler shifted Bry and [FeIII] line of D2, D23, D3, X7, X7.1, and X8. The normalized spectrum can be used to determine the [FeIII]/Br _{γ} ratio.

Appendix B: [FeIII] distribution of the D-sources

Doppler shifted [FeIII] line map

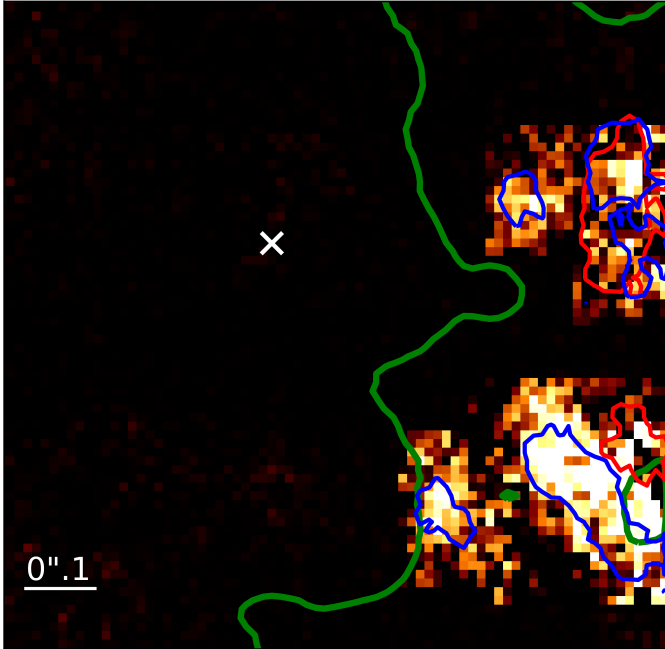


Fig. B.1. [FeIII] emission related to Fig. 6. The FOV is consistent with the mentioned figure. The investigated sources west of Sgr A* show a Doppler-shifted iron line emission that coincides with the Bry position of the D-sources.

Appendix C: Analyzed data overview

C.1. NACO data

Table C.1. Analyzed NACO data in the K- and L'-band.

NACO				
Date	Observation ID	Number of exposures	Total exposure time(s)	λ
2002.07.31	60.A-9026(A)	61	915	K
2002.08.19	60.A-9026(A)	76	2280	L'
2002.08.30	60.A-9026(A)	80	2400	L'
2003.05.10	71.B-0077(A)	56	2104	L'
2004.04.25	073.B-0840(A)	166	1743	L'
2004.04.26	073.B-0840(A)	263	3024	L'
2005.05.14	073.B-0085(D)	192	5760	L'
2006.05.29	077.B-0552(A)	522	15660	L'
2007.04.01	179.B-0261(A)	120	1800	L'
2007.05.22	079.B-0084(A)	30	450	L'
2008.05.26	081.B-0648(A)	205	3075	L'
2011.05.27	087.B-0017(A)	305	4575	K
2012.05.16	089.B-0145(A)	30	450	L'
2012.05.17	089.B-0145(A)	169	2525	K
2013.05.09	091.C-0159(A)	30	450	L'
2013.06.28	091.B-0183(A)	112	1680	K
2013.09.01	091.B-0183(B)	359	3590	K
2015.08.01	095.B-0003(A)	172	1720	K
2016.03.23	096.B-0174(A)	60	900	L'
2018.04.22	0101.B-0052(B)	120	1200	K
2018.04.24	0101.B-0052(B)	120	1200	K
2018-04-22	0101.B-0052(B)	60	1800	L'
2018-04-24	0101.B-0052(B)	50	750	L'

Notes. For every epoch, the number of exposures used for the final mosaics, the total exposure time, and the Project ID is listed. Note that NACO was decommissioned between 2013 and 2015.

C.2. SINFONI data

Table C.2. SINFONI data between 2006 and 2009.

Date (YYYY:MM:DD)	Observation ID	Start time (UT)	End time (UT)	Amount of on source exposures			Exp. time (s)
				Total	Medium	High	
2006.03.17	076.B-0259(B)	07:51:23	11:52:27	5	0	3	600
2006.03.20	076.B-0259(B)	07:33:06	07:42:27	1	1	0	600
2006.03.21	076.B-0259(B)	07:56:05	09:28:53	2	2	0	600
2006.04.22	077.B-0503(B)	08:47:59	08:57:24	1	0	0	600
2006.08.17	077.B-0503(C)	23:10:28	23:21:45	1	0	1	600
2006.08.18	077.B-0503(C)	23:19:54	03:46:01	5	0	5	600
2006.09.15	077.B-0503(C)	22:54:00	23:22:00	3	0	3	600
2007.03.26	078.B-0520(A)	06:46:26	06:57:32	1	1	0	600
2007.07.24	179.B-0261(F)	05:41:28	06:38:04	3	1	2	600
2007.09.03	179.B-0261(K)	23:42:50	01:11:12	4	1	3	600
2007.09.04	179.B-0261(K)	23:22:57	23:33:50	1	0	1	600
2008.04.06	081.B-0568(A)	05:25:26	08:50:00	16	0	15	600
2008.04.07	081.B-0568(A)	08:33:58	09:41:05	4	0	4	600
2009.05.21	183.B-0100(B)	06:10:02	08:50:36	7	0	7	600
2009.05.22	183.B-0100(B)	04:51:22	05:29:13	4	0	4	400
2009.05.23	183.B-0100(B)	09:41:41	09:57:17	2	0	2	400
2009.05.24	183.B-0100(B)	06:08:03	07:38:59	3	0	3	600

Notes. We list the total amount of data. To ensure the best S/N for our combined final data-cubes, we used only single data-cubes of high quality.

Table C.3. SINFONI data between 2010 and 2013.

Date (YYYY:MM:DD)	Observation ID	Start time (UT)	End time (UT)	Amount of on source exposures			Exp. time (s)
				Total	Medium	High	
2010.05.10	183.B-0100(O)	06:03:00	09:35:20	3	0	3	600
2010.05.11	183.B-0100(O)	03:58:08	07:35:12	5	0	5	600
2010.05.12	183.B-0100(O)	09:41:41	09:57:17	13	0	13	600
2011.04.11	087.B-0117(I)	08:17:27	09:15:16	3	0	3	600
2011.04.27	087.B-0117(I)	05:10:41	09:23:09	10	1	9	600
2011.05.02	087.B-0117(I)	07:53:34	09:22:19	6	0	6	600
2011.05.14	087.B-0117(I)	08:47:28	09:25:07	2	0	2	600
2011.07.27	087.B-0117(J)/087.A-0081(B)	02:40:51	03:30:58	2	1	1	600
2012.03.18	288.B-5040(A)	08:55:49	09:17:01	2	0	2	600
2012.05.05	087.B-0117(J)	08:09:14	08:41:33	3	0	3	600
2012.05.20	087.B-0117(J)	08:13:44	08:23:44	1	0	1	600
2012.06.30	288.B-5040(A)	01:40:19	06:54:41	12	0	10	600
2012.07.01	288.B-5040(A)	03:11:53	05:13:45	4	0	4	600
2012.07.08	288.B-5040(A)/089.B-0162(I)	00:47:39	05:38:16	13	3	8	600
2012.09.08	087.B-0117(J)	00:01:36	00:23:33	2	1	1	600
2012.09.14	087.B-0117(J)	01:21:30	01:43:27	2	0	2	600
2013.04.05	091.B-0088(A)	08:55:49	09:43:38	2	0	2	600
2013.04.06	091.B-0088(A)	07:35:58	09:23:37	8	0	8	600
2013.04.07	091.B-0088(A)	07:27:49	09:40:35	3	0	3	600
2013.04.08	091.B-0088(A)	06:42:53	09:12:52	9	0	6	600
2013.04.09	091.B-0088(A)	07:08:17	10:01:46	8	1	7	600
2013.04.10	091.B-0088(A)	06:10:45	07:47:07	3	0	3	600
2013.08.28	091.B-0088(B)	00:40:17	03:11:43	10	1	6	600
2013.08.29	091.B-0088(B)	00:46:40	03:10:00	7	2	4	600
2013.08.30	091.B-0088(B)	02:31:22	03:24:46	4	2	0	600
2013.08.31	091.B-0088(B)	00:57:58	02:28:22	6	0	4	600
2013.09.23	091.B-0086(A)	23:40:31	01:49:33	6	0	0	600
2013.09.25	091.B-0086(A)	00:39:51	01:01:39	2	1	0	600
2013.09.26	091.B-0086(A)	23:55:53	00:39:13	3	1	1	600

Table C.4. SINFONI data between 2014 and 2015.

Date (YYYY:MM:DD)	Observation ID	Start time (UT)	End time (UT)	Amount of on source exposures			Exp. time (s)
				Total	Medium	High	
2014.02.27	092.B-0920(A)	08:40:42	09:41:36	4	1	3	600
2014.02.28	091.B-0183(H)	08:34:58	09:54:37	7	3	1	400
2014.03.01	091.B-0183(H)	08:00:14	10:17:59	11	2	4	400
2014.03.02	091.B-0183(H)	07:49:05	08:18:54	3	0	0	400
2014.03.11	092.B-0920(A)	08:03:55	10:03:28	11	2	9	400
2014.03.12	092.B-0920(A)	07:44:34	10:07:45	13	8	5	400
2014.03.26	092.B-0009(C)	06:43:04	09:58:12	9	3	5	400
2014.03.27	092.B-0009(C)	06:32:49	10:04:12	18	7	5	400
2014.04.02	093.B-0932(A)	06:31:38	09:53:52	18	6	1	400
2014.04.03	093.B-0932(A)	06:20:45	09:45:02	18	1	17	400
2014.04.04	093.B-0932(B)	05:58:18	09:47:58	21	1	20	400
2014.04.06	093.B-0092(A)	07:51:42	08:43:15	5	2	3	400
2014.04.08	093.B-0218(A)	07:04:37	09:39:47	5	1	0	600
2014.04.09	093.B-0218(A)	07:43:44	09:31:25	6	0	6	600
2014.04.10	093.B-0218(A)	05:46:47	09:45:03	14	4	10	600
2014.05.08	093.B-0217(F)	05:54:04	10:13:10	14	0	14	600
2014.05.09	093.B-0218(D)	04:48:50	10:26:25	18	3	13	600
2014.06.09	093.B-0092(E)	05:22:34	08:59:59	14	3	0	400
2014.06.10	092.B-0398(A)/093.B-0092(E)	05:20:38	06:35:24	5	4	0	400/600
2014.07.08	092.B-0398(A)	02:22:28	04:47:18	6	1	3	600
2014.07.13	092.B-0398(A)	00:33:27	01:41:15	4	0	2	600
2014.07.18	092.B-0398(A)/093.B-0218(D)	02:53:11	03:03:18	1	0	0	600
2014.08.18	093.B-0218(D)	02:26:09	02:47:10	2	0	1	600
2014.08.26	093.B-0092(G)	00:23:04	01:00:16	4	3	0	400
2014.08.31	093.B-0218(B)	23:30:25	01:20:25	6	3	1	600
2014.09.07	093.B-0092(F)	01:28:11	01:42:45	2	0	0	400
2015.04.12	095.B-0036(A)	05:52:37	10:14:30	18	2	0	400
2015.04.13	095.B-0036(A)	05:44:12	10:06:37	13	7	0	400
2015.04.14	095.B-0036(A)	07:07:28	08:29:18	5	1	0	400
2015.04.15	095.B-0036(A)	05:52:26	10:16:55	23	13	10	400
2015.08.01	095.B-0036(C)	23:22:12	04:41:09	23	7	8	400
2015.09.05	095.B-0036(D)	23:18:11	02:23:03	17	11	4	400

Appendix D: K- and L-band positions of the D-sources**Table D.1.** K-band positions of D2, D23, D3, and D3.1 extracted from the NACO data between 2002 and 2018.

Date	D2 positions		D23 positions		D3 positions		D3.1 positions	
	Δ RA [mas]	Δ Dec [mas]	Δ RA [mas]	Δ Dec [mas]	Δ RA [mas]	Δ Dec [mas]	Δ RA [mas]	Δ Dec [mas]
2002.578	–	–	-324.76 ± 13.0	126.33 ± 13.0	–	–	–	–
2003.446	–	–	-306.36 ± 6.5	125.18 ± 6.5	–	–	–	–
2004.661	–	–	-347.65 ± 13.0	99.29 ± 13.0	–	–	–	–
2004.669	–	–	-336.28 ± 13.0	101.88 ± 13.0	–	–	–	–
2004.726	–	–	-347.47 ± 6.5	97.07 ± 6.5	–	–	–	–
2005.268	–	–	-350.00 ± 6.5	108.94 ± 6.5	–	–	–	–
2005.369	–	–	-376.69 ± 6.5	134.30 ± 6.5	–	–	–	–
2005.372	–	–	-332.92 ± 6.5	133.15 ± 6.5	–	–	–	–
2005.567	–	–	-362.95 ± 6.5	135.83 ± 6.5	–	–	–	–
2007.213	–	–	-396.50 ± 13.0	152.04 ± 13.0	–	–	–	–
2007.252	–	–	-397.15 ± 13.0	137.21 ± 13.0	–	–	–	–
2007.454	–	–	-396.20 ± 13.0	139.59 ± 13.0	–	–	–	–
2008.144	-464.92 ± 13.0	-93.8 ± 13.0	-414.26 ± 6.5	125.75 ± 6.5	-566.92 ± 10.44	-23.80 ± 16.53	–	–
2008.196	-471.79 ± 13.0	-82.21 ± 13.0	-425.79 ± 6.5	114.30 ± 6.5	-573.79 ± 15.08	-12.21 ± 19.31	–	–
2008.267	-470.03 ± 13.0	-98.59 ± 13.0	-419.38 ± 13.0	112.26 ± 13.0	-572.03 ± 14.14	-28.59 ± 17.84	-501.0 ± 15.0	33.0 ± 15.0
2008.456	-469.78 ± 13.0	-85.77 ± 13.0	-428.69 ± 6.5	122.64 ± 6.5	-571.78 ± 11.70	-15.77 ± 21.62	–	–
2008.598	-466.08 ± 13.0	-86.89 ± 13.0	-424.97 ± 13.0	132.002 ± 13.0	-568.08 ± 15.63	-16.89 ± 23.87	–	–
2008.707	-471.37 ± 13.0	-85.80 ± 13.0	-428.17 ± 6.5	126.80 ± 6.5	-573.37 ± 14.28	-15.80 ± 21.09	–	–
2009.298	-459.5 ± 6.5	-45.33 ± 6.5	-424.62 ± 13.0	126.70 ± 13.0	-575.50 ± 17.16	10.67 ± 17.78	–	–
2009.301	-457.08 ± 6.5	-48.45 ± 6.5	-424.89 ± 13.0	123.67 ± 13.0	-573.08 ± 13.05	7.55 ± 21.82	–	–
2009.334	449.71 ± 6.5	-40.40 ± 6.5	-430.34 ± 6.5	127.57 ± 6.5	-565.71 ± 16.91	15.60 ± 18.24	–	–
2009.369	–	–	-461.24 ± 13.0	-62.54 ± 13.0	–	–	–	–
2009.501	-457.89 ± 13.0	-40.45 ± 13.0	-428.58 ± 13.0	117.76 ± 13.0	-573.89 ± 15.60	15.55 ± 19.01	–	–
2009.509	–	–	-424.48 ± 6.5	112.95 ± 6.5	–	–	–	–
2009.611	-449.71 ± 6.5	-40.40 ± 6.5	-430.93 ± 6.5	130.90 ± 6.5	-565.71 ± 16.12	15.60 ± 23.99	–	–
2009.715	-439.88 ± 13.0	-33.22 ± 13.0	-426.42 ± 13.0	127.02 ± 13.0	-555.88 ± 17.43	22.78 ± 26.15	–	–
2009.717	-457.22 ± 13.0	-48.24 ± 13.0	-424.87 ± 13.0	133.18 ± 13.0	-573.22 ± 19.22	7.76 ± 23.45	–	–
2010.350	-454.89 ± 6.5	-45.43 ± 6.5	-483.54 ± 6.5	105.78 ± 6.5	-570.89 ± 15.25	10.57 ± 24.73	-519.0 ± 15.0	33 ± 15.0
2010.454	-457.76 ± 6.5	-35.38 ± 6.5	-484.46 ± 6.5	109.42 ± 6.5	-573.76 ± 17.43	20.62 ± 25.42	–	–
2011.400	-455.53 ± 6.5	-25.50 ± 6.5	-486.99 ± 6.5	134.24 ± 6.5	-599.53 ± 20.58	30.50 ± 26.21	-466 ± 15.0	51 ± 15.0
2012.374	-401.66 ± 6.5	-8.35 ± 6.5	-477.94 ± 6.5	105.63 ± 6.5	-573.66 ± 17.22	47.65 ± 21.18	–	–
2013.487	-412.51 ± 13.0	11.67 ± 13.0	-465.00 ± 6.5	131.23 ± 6.5	-556.51 ± 20.25	39.67 ± 23.61	–	–
2013.670	–	–	-506.79 ± 6.5	131.93 ± 6.5	–	–	–	–
2015.580	-390.97 ± 13.0	61.57 ± 13.0	-537.93 ± 6.5	126.65 ± 6.5	-576.97 ± 19.99	61.57 ± 27.15	–	–
2018.306	-307.31 ± 13.0	120.87 ± 13.0	-553.72 ± 6.5	122.33 ± 6.5	-549.31 ± 22.36	106.87 ± 24.55	–	–

Table D.2. Positions of D2, D23, D3, and D3.1 from the *L*-band NACO data set.

Date	D2 positions		D23 Positions		D3 Positions		D3.1 Positions	
	ΔRA [mas]	ΔDec [mas]	ΔRA [mas]	ΔDec [mas]	ΔRA [mas]	ΔDec [mas]	ΔRA [mas]	ΔDec [mas]
2002.66	-500.58 ± 5.64	-176.85 ± 5.51	–	–	-612.58 ± 10.44	-36.85 ± 16.53	–	–
2002.72	-497.88 ± 4.77	-180.9 ± 5.21	–	–	-609.88 ± 15.08	-40.90 ± 19.31	–	–
2002.75	-487.08 ± 4.42	-182.79 ± 4.92	-338.85 ± 13.6	119.47 ± 13.6	-599.08 ± 14.14	-42.79 ± 17.84	–	–
2002.83	-497.88 ± 5.04	-183.6 ± 5.62	–	–	-609.88 ± 11.70	-43.60 ± 21.62	–	–
2003.44	-491.13 ± 3.99	-176.58 ± 4.66	-385.95 ± 13.6	113.85 ± 13.6	-603.13 ± 15.63	-64.58 ± 23.87	–	–
2004.32	-485.73 ± 2.49	-151.47 ± 8.54	–	–	-611.73 ± 14.28	-39.47 ± 21.09	-550.73 ± 15.0	-8.47 ± 15.0
2004.40	-482.76 ± 4.04	-155.79 ± 4.76	-363.19 ± 13.6	119.24 ± 13.6	-608.76 ± 17.16	-43.79 ± 17.78	–	–
2004.41	-481.41 ± 4.52	-159.57 ± 6.70	-346.50 ± 13.6	118.68 ± 13.6	-607.41 ± 13.05	-47.57 ± 21.82	–	–
2005.45	-485.19 ± 4.50	-133.92 ± 9.99	-374.66 ± 13.6	126.32 ± 13.6	-611.19 ± 16.91	-21.92 ± 18.24	-602.19 ± 15.0	-16.92 ± 15.0
2005.54	-482.49 ± 5.46	-124.47 ± 5.92	–	–	-608.49 ± 15.60	-12.47 ± 19.01	–	–
2006.50	-473.85 ± 4.86	-110.43 ± 4.65	-394.80 ± 13.6	126.32 ± 13.6	-599.85 ± 16.12	-12.43 ± 23.99	-590.85 ± 15.0	-6.43 ± 15.0
2007.34	-460.62 ± 4.59	-99.36 ± 3.65	-416.99 ± 13.6	126.27 ± 13.6	-572.62 ± 17.43	-15.36 ± 26.15	-603.62 ± 15.0	34.36 ± 15.0
2007.48	-461.43 ± 3.09	-96.12 ± 2.75	-403.1 ± 13.6	134.58 ± 13.6	-573.43 ± 19.22	-12.12 ± 23.45	–	–
2008.49	-453.33 ± 5.92	-79.38 ± 6.93	-432.47 ± 13.6	129.57 ± 13.6	-579.33 ± 15.25	18.62 ± 24.73	–	–
2011.40	-433.35 ± 10.09	-41.04 ± 11.66	–	–	-545.35 ± 17.43	14.96 ± 25.42	–	–
2011.49	-416.07 ± 11.86	-34.02 ± 12.94	-479.54 ± 13.6	139.92 ± 13.6	-528.07 ± 20.58	21.98 ± 26.21	–	–
2012.46	-423.63 ± 9.37	-8.1 ± 12.31	-468.76 ± 13.6	141.17 ± 13.6	-535.63 ± 17.22	61.90 ± 21.18	-405.0 ± 15.0	25.0 ± 15.0
2013.44	-414.99 ± 10.04	23.76 ± 13.49	-484.57 ± 13.6	135.39 ± 13.6	-540.99 ± 20.25	79.76 ± 23.61	–	–
2016.31	-370.44 ± 7.04	86.67 ± 9.93	-519.09 ± 13.6	114.32 ± 13.6	-510.44 ± 19.99	114.67 ± 27.15	–	–
2018.39	-343.98 ± 7.24	123.66 ± 10.27	-510.75 ± 13.6	121.32 ± 13.6	-539.98 ± 22.36	137.66 ± 24.55	–	–
2018.40	-343.17 ± 6.39	125.55 ± 10.62	-514.39 ± 13.6	136.87 ± 13.6	-539.17 ± 18.45	139.55 ± 29.51	–	–

Appendix E: Bubble around Sgr A* - a NIR/Radio connection

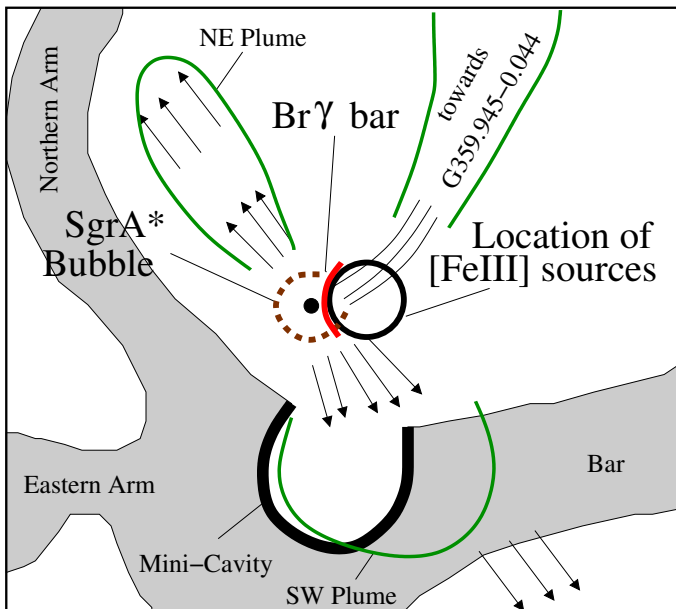


Fig. E.1. Image inspired by the results presented in Yusef-Zadeh et al. (2012). It shows the radio emission and the detected features. We indicate the position of the bright Br γ -emission with a red bar at the position of the open Sgr A* bubble. The black circle marks the position of the dusty sources that show Doppler-shifted [FeIII] emission lines.

Appendix F: *H*- and *K*-band detection of the DSO/G2 object

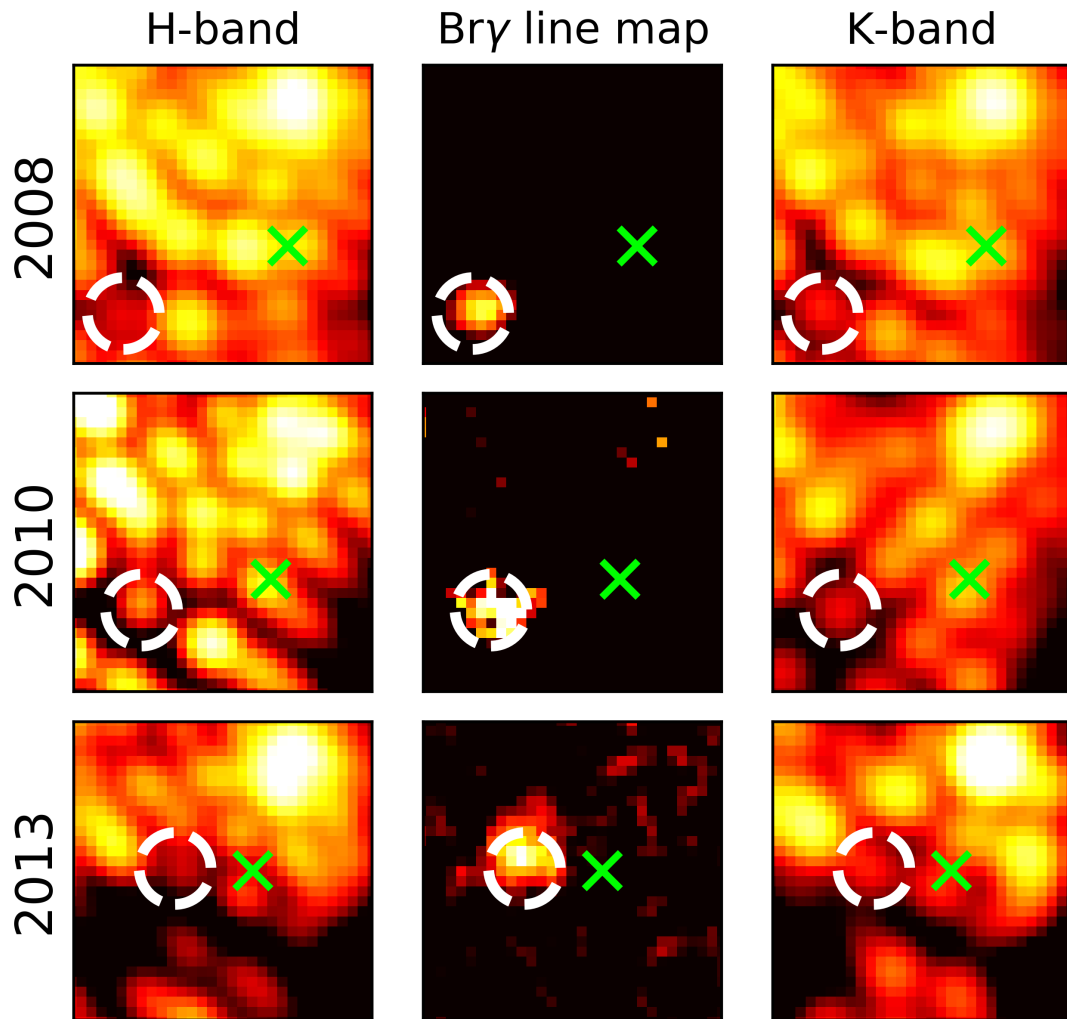


Fig. F.1. *H*-, *K*-band detection of the DSO. For a positional comparison, we include the Doppler-shifted line-map detection. The data is based on the SINFONI *H* + *K* data-cubes of 2008, 2010, and 2013. In all images, north is up and east is to the left. Sgr A* is marked with a lime-colored *x*. The FOV in every image is $0''.375 \times 0''.375$.